JGR Space Physics

Key Points:
- A sheath interplanetary counterpart of a solar coronal mass ejection (ICME) crossing drives conditions for an electron flux dropout
- Ultralow frequency (ULF), electromagnetic ion cyclotron, and chorus waves were excited after the interplanetary shock and only ULF and chorus waves persisted during the magnetic cloud
- Resonant wave-particle interactions seem to be effective only during the turbulent ICME's sheath region

Supporting Information:
- Supporting Information S1

Correspondence to:
L. A. Da Silva,
ligia.alves01@gmail.com; ligia.silva@inpe.br

Dynamic Mechanisms Associated With High-Energy Electron Flux Dropout in the Earth's Outer Radiation Belt Under the Influence of a Coronal Mass Ejection Sheath Region

L. A. Da Silva[1,2] , J. Shi[1], L. R. Alves[2] , D. Sibeck[3] , V. M. Souza[2] , J. P. Marchezi[2] , C. Medeiros[2] , L. E. A. Vieira[2] , O. Agapitov[4] , P. R. Jauer[1,2] , M. E. S. Alves[5], C. Wang[1] , H. Li[1], Z. Liu[1], A. Dal Lago[2] , M. V. Alves[2], M. S. Rockenbach[2], D. N. Baker[6] , S. Y. Zhang[7], and S. G. Kanekal[3]

[1]National Space Science Center, State Key Laboratory of Space Weather, Chinese Academy of Sciences, Beijing, China, [2]National Institute for Space Research—INPE, São José dos Campos, SP, Brazil, [3]NASA Goddard Space Flight Center, Greenbelt, MD, USA, [4]Space Science Laboratory, University of California, Berkeley, CA, USA, [5]Universidade Estadual Paulista-UNESP, Instituto de Ciência e Tecnologia, São José dos Campos, SP, Brazil, [6]Laboratory for Atmosphere and Space Physics—LASP, Boulder, CO, USA, [7]National Space Science Center, Chinese Academy of Sciences, Beijing, China

Abstract The near-Earth interplanetary environment conditions affect the dynamics of the relativistic electron population quasitrapped in the radiation belts. A complex chain of processes observed in the magnetosphere can contribute to the variability of these populations when interplanetary structures, such as the interplanetary counterpart of a solar coronal mass ejection (ICME), and high-speed solar wind streams interact with the magnetosphere. However, as these processes can coexist, it is hard to untangle the relative contribution of each process to the loss of particles and the eventual repopulation. Here we show evidence that it is possible to distinguish the relative contribution of mechanisms related to the loss of the outer radiation belt electrons for an event observed on July 19 and 20, 2016. The interaction of an ICME's turbulent sheath with the Earth's magnetosphere resulted in a decrease in the outer radiation belt relativistic electron population. The ultralow frequency (ULF) and chorus wave activities are detected in the outer radiation belt during the time when the Earth's magnetosphere is under the influence of the ICME's sheath region, as well as the ICME's magnetic cloud region, while the electromagnetic ion cyclotron (EMIC) waves in the outer belt are observed only during the sheath region. Dynamic mechanisms such as magnetopause shadowing, outward radial diffusion driven by ULF waves, pitch-angle scattering driven by both EMIC and chorus waves are quantitatively analyzed. Our results suggest that the structures of the ICMEs can trigger the drivers to generate the different dynamic mechanisms responsible for the radiation belt population variability.

1. Introduction

Electron fluxes in the outer radiation belt are essentially governed by the dynamics of trapped particle motion in the inner magnetosphere, wherein the energetic particles execute complex periodic motions. Each motion is associated with one adiabatic invariant, namely, gyromotion around the magnetic field line, which is described as the first adiabatic invariant, bounce motion along the magnetic field line being identified as the second adiabatic invariant, and drift motion around the Earth as the third adiabatic invariant (Northrop & Teller, 1960; Roederer, 1970). Early spacecraft data revealed that phase space densities across the belts can vary significantly with time (see Roederer 1968), in which the violation of one or more adiabatic invariants can be required. This violation can occur due to the presence of several electrodynamic and magnetohydrodynamic processes in the magnetosphere, causing variations in the outer radiation belt electron flux, such as dropouts (e.g., Alves et al., 2017; Turner et al. 2012; Turner & Ukhorskiy, 2019), and enhancements (e.g., Baker et al., 1994, 2014; Baker & Kanekal, 2008; Boyd et al., 2018; Da Silva et al., 2019). Usually, it is hard to distinguish the dominant process leading to outer belt electron flux variability when several of them are acting at the same time.

The different electrodynamic and magnetohydrodynamic processes in the magnetosphere that are able to violate the adiabatic invariants can take place when solar wind structures reach the Earth, like High-Speed solar wind Streams (HSS) and Interplanetary Coronal Mass Ejections (ICME; Tsurutani & Lakhina, 2014). The variability of the outer radiation belt electron flux is driven by a complex chain of processes extending from the solar wind into the inner magnetosphere (e.g., Kalliokoski et al., 2020; Nagai, 1988; Paulikas & Blake, 1979). Solar wind structures such as ICME are the ones usually with the strongest intensity since its origin in the solar corona (Burlaga et al., 1981). Consequently, the deposit of energy in the magnetosphere will occur with greater intensity, compared to other solar wind structures and quiet periods (Ponomarev et al., 2006). The energy delivered to the magnetosphere is considerably larger during ICME occurrences, which may cause strong compression of the magnetopause. Among the consequences of this impact, it is possible to detect the outer radiation belt flux decrease as abrupt dropouts.

Due to the ICME's impingement on the geomagnetic field, electromagnetic waves over a wide range of frequencies can be excited in the magnetosphere, both during and after the ICME occurrence, such as ultralow frequency (ULF) waves (a few milihertz up to about 5 Hz) (e.g., Kivelson & Southwood, 1985; Mann et al., 1999), electromagnetic ion cyclotron (EMIC) waves (0.2 up to 5 Hz) (e.g., Horne, 2002; Medeiros et al., 2019; Thorne, 2010), and whistler mode chorus waves (hundreds of Hz up to about 10 kHz) (e.g., Alves et al., 2016; Gurnett & O'Brien, 1964). Dynamic mechanisms related to wave-particle interaction processes, such as radial diffusion and pitch angle scattering can occur during the aforementioned wave activities, and they can be, in turn, associated with either losses or replenishments of the outer radiation belt electron flux.

The ICMEs' signatures are distinguished from the ambient solar wind by specific plasma, compositional, and magnetic field signatures (e.g., Zurbuchen & Richardson, 2006), on average. When an ICME is sufficiently faster than the preceding solar wind, a shock wave develops ahead of the ICME, generating a turbulent region between the shock and the ICME, called the sheath region (See E. Kilpua et al., 2017). The sheath region is a turbulent and compressed structures with large amplitude magnetic field variations and high dynamic pressure. The ICME with Sheath region drives practically all intense geomagnetic storms (E. Kilpua et al., 2017), which enable effective magnetic reconnection at the magnetopause when their magnetic field has a strong southward component.

Although the literature shows that the most important drivers of geomagnetic activity are the ICMEs and sheath regions, the approach extensively studied by the scientific community is the geomagnetic storm response in the outer radiation belt flux variability (Reeves et al., 2013; Turner et al., 2013, 2014), without considering the driver. A recent statistical study showed that the turbulent sheath regions preceding ICMEs can cause significant changes in the outer radiation belt electron fluxes during both nongeoeffective and dramatic geoeffective sheaths (Kalliokoski et al., 2020). This specific statistical study motivates the scientific community to investigate in detail the response of the outer radiation belt flux to sheath regions of ICMEs during both weak and moderate geomagnetic storms. Therefore, this work analyzes the outer radiation belt response to the sheath region of an ICME during a sudden commencement storm, classified as a moderate geomagnetic storm, in which the dynamic mechanisms are identified and quantified during the influence of the turbulent ICME sheath region.

This work is divided into the following sections: instrumentation (Section 2); description of the observations employed (Section 3); the dynamical processes likely responsible for the electron flux variability in the outer radiation belt (Section 4); discussion about Section 4 through pitch angle distribution and time evolution of phase space density radial profiles (Section 5), and finally the conclusions (Section 6).

2. Instrumentation

Satellite and ground-based data are employed for the development of this study. The radiation belt electron flux is studied using data from both the Relativistic Electron-Proton Telescope (Baker et al., 2013) and Magnetic Electron Ion Spectrometer (Blake et al., 2013) instruments onboard Van Allen Probes A and B (Mauk et al., 2012), and also from the Space Weather Suite/Space Environment Monitor/High Energy Particle Detector (SWS/SEM/HEPD) data onboard FengYun series spacecraft 3C (S. Y. Zhang et al., 2014). Van Allen

Probes′ mission had a highly elliptical geocentric orbit with a perigee altitude of 618 km, and an apogee altitude of 30,414 km. Their inclination was 10.2°, and the orbit period was 537.1 min. FengYun 3C is the third flight unit of the FY-3 satellite series. Their orbit is sun-synchronous (Low Earth orbit), quasipolar, constant equatorial time, and altitude 831 km.

Solar wind parameters at the L1 Lagrangian point are acquired from the Magnetic Field Experiment (MAG) instrument with a temporal resolution of 5 min, and the Solar Wind Electron, Proton, and Alpha Monitor (SWEPAM) instrument with a temporal resolution of 5 min. Both detectors are onboard the Advanced Composition Explorer (ACE, Stone et al., 1998) spacecraft. Solar wind parameters are also acquired from three-dimensional plasma and energetic particle investigation (3DP) instrument onboard the WIND spacecraft (Ogilvie et al., 1995).

ULF, EMIC, and chorus wave power spectral densities were calculated using data from the Electric and Magnetic Field Instrument Suite and Integrated Science (EMFISIS, Kletzing et al., 2013) instrument onboard the Van Allen Probes. ULF wave power spectral densities were also calculated from the International Monitor for Auroral Geomagnetic Effects (IMAGE) ground magnetometer network (Viljanen & Hakkinen, 1997).

3. Overview of the Interplanetary Conditions and the Overall Response of the Magnetosphere

The Earth's magnetosphere is embedded in the Solar Atmosphere. In this way, changes in the structure of the solar wind trigger a wide range of disturbances in the magnetosphere collectively known as magnetic storms (Gonzalez et al., 1994). This section, describes the conditions of the solar wind, and the overall response of the magnetosphere from July 19, 2016 12:00 Universal Time (UT) to July 23, 2016 00:00 UT.

Figure 1 presents an overview of the interplanetary conditions measured by instrumentation onboard the ACE spacecraft, orbiting the Lagrangian point L1. In Figures 1a and 1b, we present the solar wind speed and density, respectively. The blue lines are 5-min averages from ACE spacecraft. As solar wind density at a level-2 calibration for the ACE spacecraft is not available, we also show for reference 1-h averages from Wind spacecraft (red lines). Panel (1c) presents the total magnetic field (Bt) and the z component of the interplanetary magnetic field (IMF) in the Geocentric solar magnetospheric (GSM) coordinate system. Panel (1d) displays the x and y components of the IMF, also in GSM.

The dashed line S1 indicates the occurrence of shock in the interplanetary medium on July 19, 2016 23:05 UT. The boundary of the ICME can be estimated based on plasma and magnetic field observations (e.g., Burlaga et al., 1981; Cane & Richardson, 2003; Kilpua et al., 2013). The dashed lines MC1 and MC2 show the boundaries of the following interplanetary magnetic cloud observed on July 20, 2016 07:00 UT and July 22, 2016 15:00 UT, respectively.

It is possible to observe just behind the shock S1, in the ICME sheath region, an intense north-south IMF Bz component reaching approximately −26 nT that seems to be a consequence of the draping of the magnetic field around the ejecta. The solar wind velocity reaches a maximum of approximately 600 km/s near the leading edge of the magnetic cloud (MC1). A density peak of approximately 50 #/cm^3 was observed just behind the shock S1.

We present in Figure 1e the symmetric geomagnetic index (Sym-H), which is a proxy of the global response of the near equatorial current systems. An impulse, denoted by the vertical dotted bar marked as SC occurred on July 19, 2016 at 23:50 UT. The travel time from the ACE spacecraft to the magnetopause was approximately 45 min. The increase in the Sym-H index reached a maximum of 52 nT was caused by the enhancement of the Chapman-Ferraro current system due to the rise of the solar wind pressure (not shown). The Sym-H Index remained at this level until 01:05 UT on July 20, 2016. The ring current build-up caused a monotonic decrease of the Sym-H index. This decrease is the signature of the main phase of the magnetic storm that lasted until 07:00 UT on July 20, 2016 when the Sym-H index reached its lowest value of approximately −32 nT.
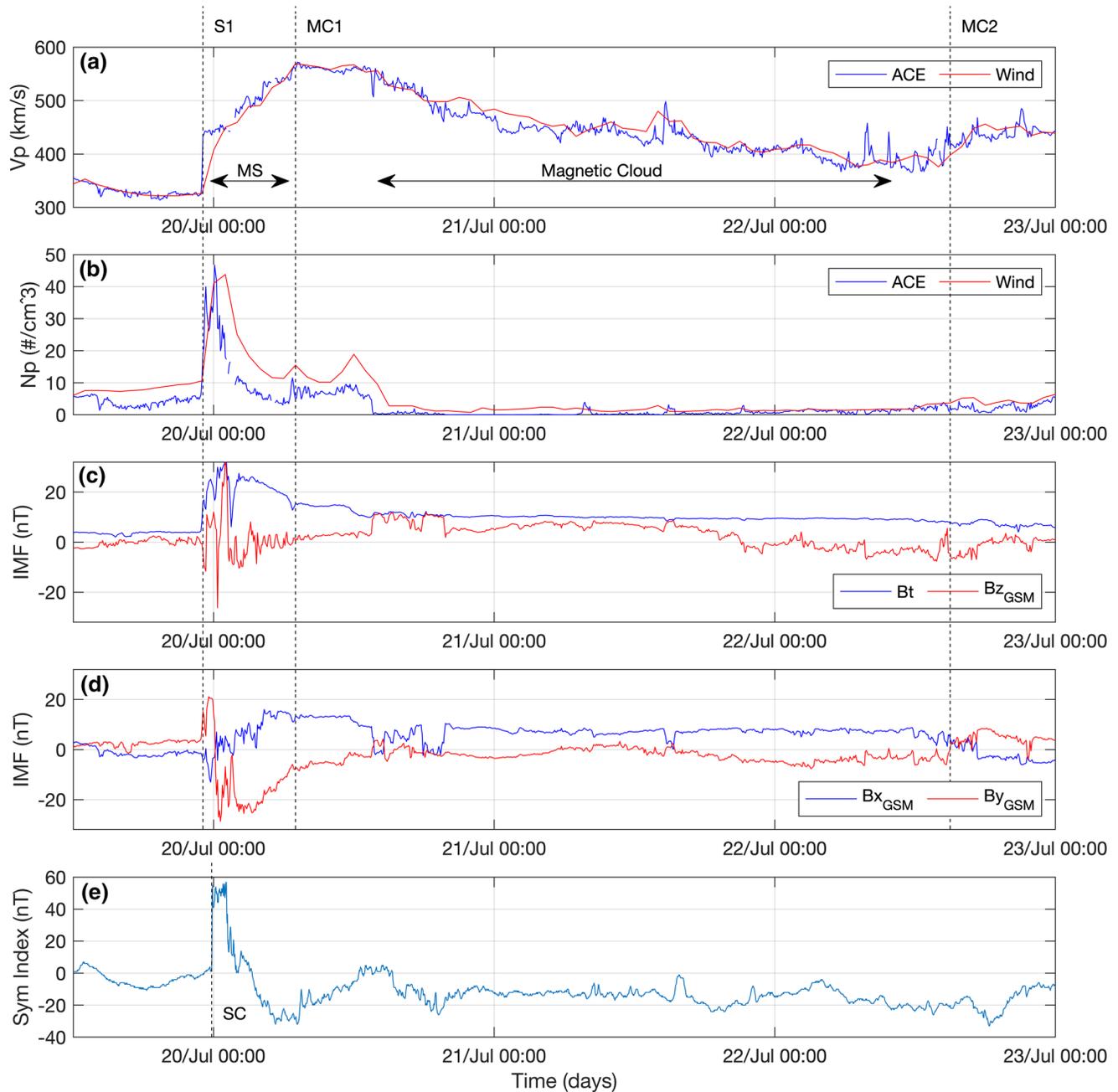
Figure 1. (a) solar wind speed (Vp); (b) density (Np); (c) Interplanetary Magnetic Field (IMF) intensity (Bt) and Bz component; (d) IMF Bx (blue) and By (red) components; (e) symmetric geomagnetic index (Sym-H) obtained from the OMNI database. The Vp (blue line), Np (blue line), Bt, Bz, Bx and By are obtained by ACE satellite in the Lagrangian L1 point. The Vp (red line), Np (red line) are obtained by the WIND satellite in the Lagrangian L1 point. The dashed line S1 indicates the occurrence of the interplanetary shock on July 19, 2016 at 23:05 UT. The dashed lines MC1 and MC2 show the boundaries of the following interplanetary magnetic cloud observed on July 20, 2016 at 07:00 UT and July 22, 2016 at 15:00 UT, respectively. The dashed line SC indicates the sudden commencement impulse occurred on July 19, 2016 at 23:50 UT. The MS indicates the ICME's magnetosheath. ICME, interplanetary counterpart of a solar coronal mass ejection.

We present in panels (a) and (b) of Figure 2 the electron flux at 2.10 MeV energy as a function of L-shell (vertical axis) and time (horizontal axis) for Van Allen Probes A and B, respectively. The L-shell is more fit to be used with flux data as fluxes are not conserved (Reeves et al., 2013). To improve the visualization of the fluxes, we employ a triangulation-based linear interpolation with a uniform grid with a time interval
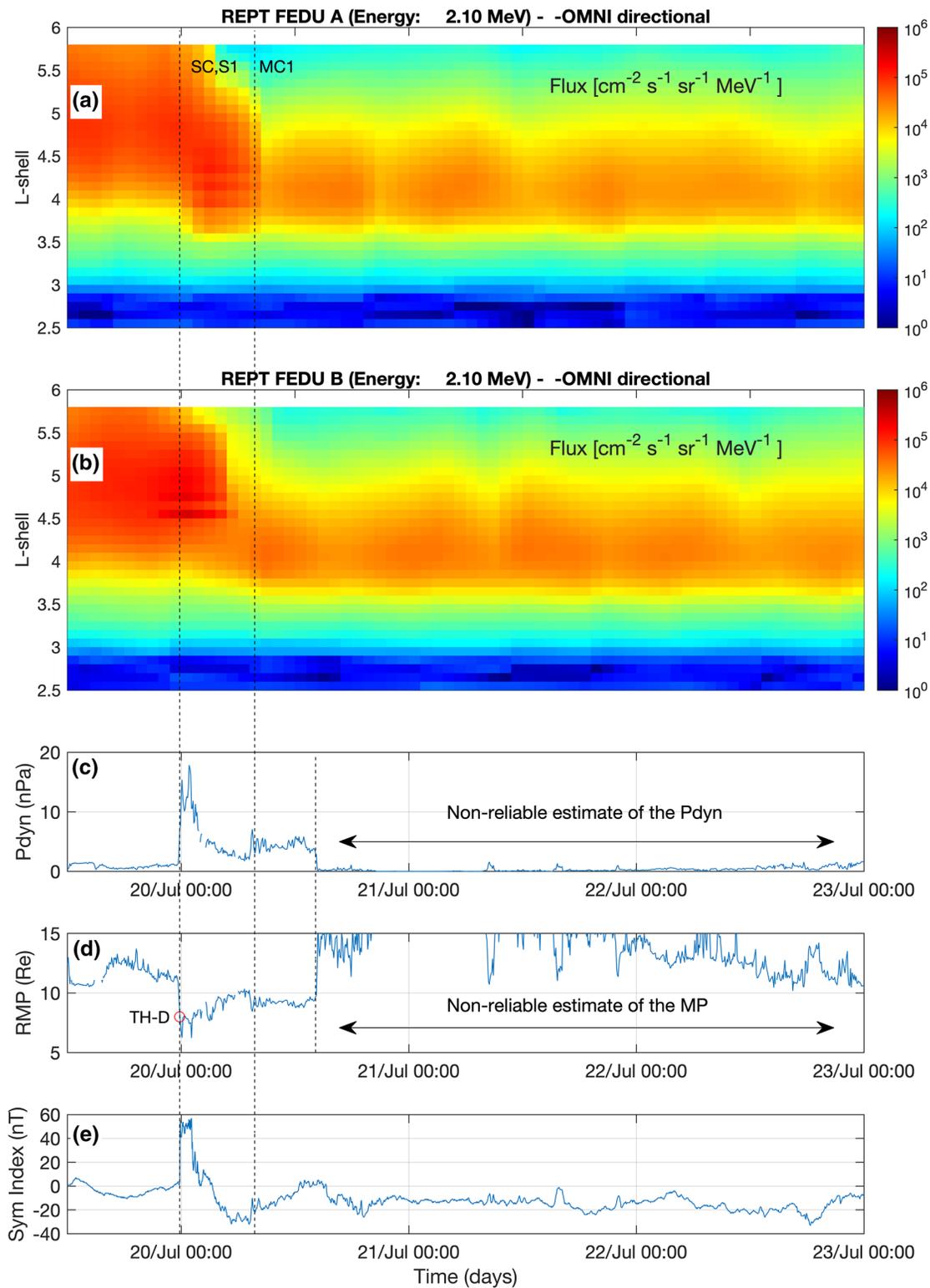
Figure 2. (a and b) Electron flux at 2.10 MeV energy as a function of L-shell (vertical axis) and time (horizontal axis) for the Van Allen Probe A and B, respectively; (c) solar wind dynamic pressure calculated from ACE satellite data; (d) magnetopause stand-off distance by the Shue et al., (1998) model; (e) symmetric geomagnetic index (Sym-H) obtained from the OMNI database. The dashed line SC indicates the sudden commencement impulse occurred on July 19, 2016 at 23:50 UT, in which the S1 time was shifted to coincide to the SC time. The dashed line MC1 shows the following interplanetary magnetic cloud boundary, in which MC1 time was shifted to the time-lagged one (07:45 UT). TH-D represents the spacecraft THEMIS-D crossing magnetopause at ~23:50 UT (x-GSE ~8RE).
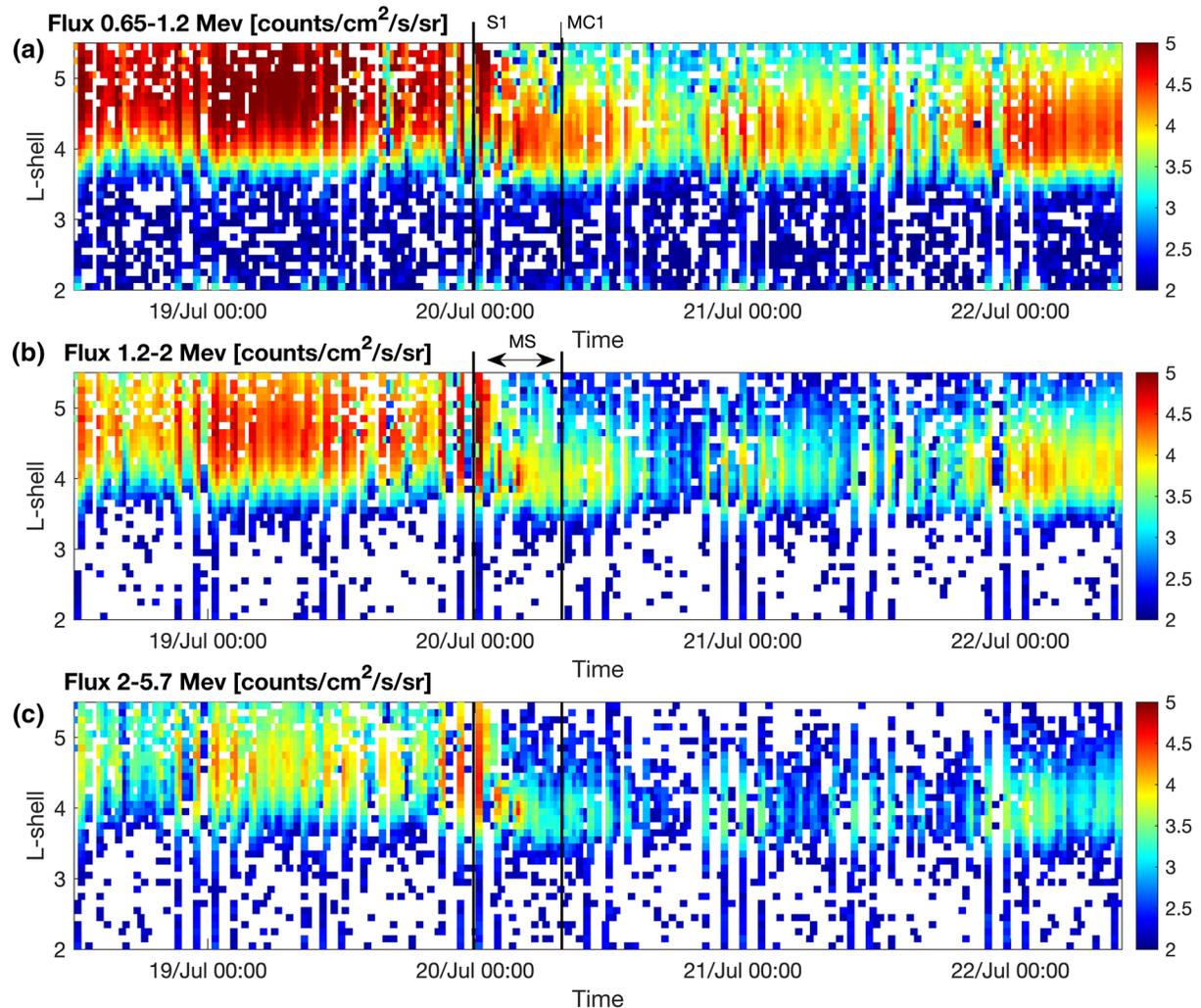
Figure 3. Electron fluxes at 0.65–1.2 MeV (upper panel), 1.2–2 MeV (middle) and 2–5.7 MeV (bottom) energies as a function of L-shell (vertical axis) and time (horizontal axis) observed by low-orbit FengYun 3C spacecraft. The color scale specifies the logarithmic values of electron fluxes (counts/cm^2/s/sr).

of 72 min and a parameter L interval of 0.1, a method widely used by the scientific community of this area (e.g., Alves et al., 2016; Da Silva et al., 2019; Souza et al., 2017). Figures 2c and 2d display the solar wind dynamic pressure and the magnetopause standoff distance, respectively. The magnetopause standoff distance, which is a crucial parameter for understanding the dropout of high-energy particles quasitrapped in the outer radiation belt, was estimated by employing the empirical model of Shue et al. (1998). We indicate in Figures 2c and 2d the period when the estimates of the solar wind dynamic pressure and the standoff distance are not reliable. The period not reliable is due to the limitation of the empirical model regarding the interplanetary medium data, in which the proton density is approximately zero.

Here we focus on the region between the shock and the leading edge of the magnetic cloud, the turbulent sheath region. For reference, the dashed lines (Figure 2) show the sudden commencement impulse (SC) and the time-lagged leading edge of the magnetic cloud. A visual inspection in Figure 2 suggests that the high-energy electron flux (2.1 MeV energy channel) decreased significantly, by three orders of magnitude from L-shell = 4.7 to 6 and by two orders of magnitude below L-shell = 4.7, during the passage of the turbulent ICME magnetosheath region (see Figure S2—non interpolated version).

Figure 3 presents the electron fluxes at 0.65–1.2, 1.2–2, and 2–5.7 MeV energies as a function of L-shell (vertical axis) and time (horizontal axis) observed by the low-orbit FengYun 3C spacecraft (the orbital effects

are present in Figure 3). Although the Van Allen Probes (equatorial orbit) and FengYun series spacecraft 3C (Sunsyncronous orbit) make different orbits, visual inspection in Figure 3 also suggests that the high-energy electron flux (>1 MeV) dropout occurred during the time when the Earth's magnetosphere was under the influence of the turbulent ICME's sheath region, presenting a significant flux decrease above L-shell = 4.7 and below L-shell = 4.6.

High-energy electron flux (1.8, 2.10, 2.6, and 3.4 MeV) available from the Van Allen Probe B (Figure 4), obtained at $L^* = 5.2$ and 4.6 provide details regarding the flux dropout that occurred under the influence of the turbulent ICME's sheath region. At $L^* = 5.2$ the flux dropout was observed after 21:56 UT, while at $L^* = 4.6$ the flux dropout was observed after 22:45 UT.

4. Dynamic Mechanisms Associated with the High-Energy Electron Flux Dropout

The conditions of the solar wind during the analyzed period are favorable to compress the dayside magnetopause and excite magnetospheric waves in a wide range of frequencies. As noted by Xiang et al., (2017), during the fast dropouts, the radiation belt electrons can be lost either by transport across the magnetopause into the interplanetary space or by precipitation into the atmosphere. The scientific community presently accepts, that both magnetopause shadowing combined with outward radial diffusion, and the particle precipitations into the atmosphere due to wave-induced pitch angle scattering can contribute to radiation belt dropouts (e.g., X. Li et al., 1997; Morley et al., 2010; Tu et al., 2010; D. L. Turner et al., 2012).

The recent statistical evidence and series of new observational results from in-depth case studies revised by Turner and Ukhorskiy (2019) show that the community is still somewhat divided on exactly how and why losses in some outer belt dropout events are dominated by magnetopause incursions and enhanced outer radial transport while others are dominated by losses from interactions with EMIC waves. Therefore, it is important to investigate in detail both magnetopause shadowing and the wave-particle interaction mechanisms. The following sections address this point.

4.1. Magnetopause Shadowing

Magnetopause shadowing occurs when higher solar wind dynamic pressure compresses the magnetopause (Herrera et al., 2016; Wilken et al., 1982). The compression normally is associated with solar wind structures, which are able to perturb and inject energy on the Earth's magnetosphere (Gonzalez et al., 1994). We use the empirical model of Shue et al. (1998) and the Space Weather Modeling Framework/Block-Adaptive-Tree Solar-Wind Roe-Type Upwind Scheme (SWMF/BATS-R-US) global MHD model (De Zeeuw et al., 2004; Gombosi, et al., 2004; Tóth et al., 2012; Tóth et al., 2005; Powell et al., 1999; Ridley and Liemohn et al., 2002; Wolf et al., 1977) developed at the University of Michigan in the Center for Space Environment Modeling (CSEM) to estimate the magnitude of the compression.

Figure 5d presents the empirical model results. A strong dayside magnetopause compression can be seen at ~23:05 UT on July 19th, with the modeled stand-off distance reaching ~6 R_E, suggesting that the magnetopause reached the outskirts of the outer radiation belt. Global magnetic field compression generally induces an impulsive electric field in the azimuthal direction, which can play an essential role in accelerating and transporting radiation belt electrons (D. Zhang et al., 2018). This compression is observed almost simultaneously with the ICME's shock signatures, namely, an abrupt increase in the solar wind velocity (Figure 5b) and IMF strength and an abrupt decrease in the north-south component Bz (Figure 5c). Also, the magnetopause compression occurred nearly simultaneously with the sudden ~ three orders of magnitude decrease of the relativistic electron flux in $L^* = 5.2$ (Figure 5a). These results suggest that the magnetopause shadowing mechanism contributed to the loss of high-energy (relativistic) electrons.

A global MHD simulation of the Earth's magnetosphere interaction with the ICME on July 19, 2016, has been performed to confirm again the likelihood of magnetopause shadowing occurrence. The simulation setup is similar to that done by Alves et al. (2016) and Da Silva et al. (2019). The whole simulation domain is set with the following dimensions $-224 \leq x \leq 32$ RE, and $-64 \leq y, z \leq 64$ RE, where x, y, and z are in the
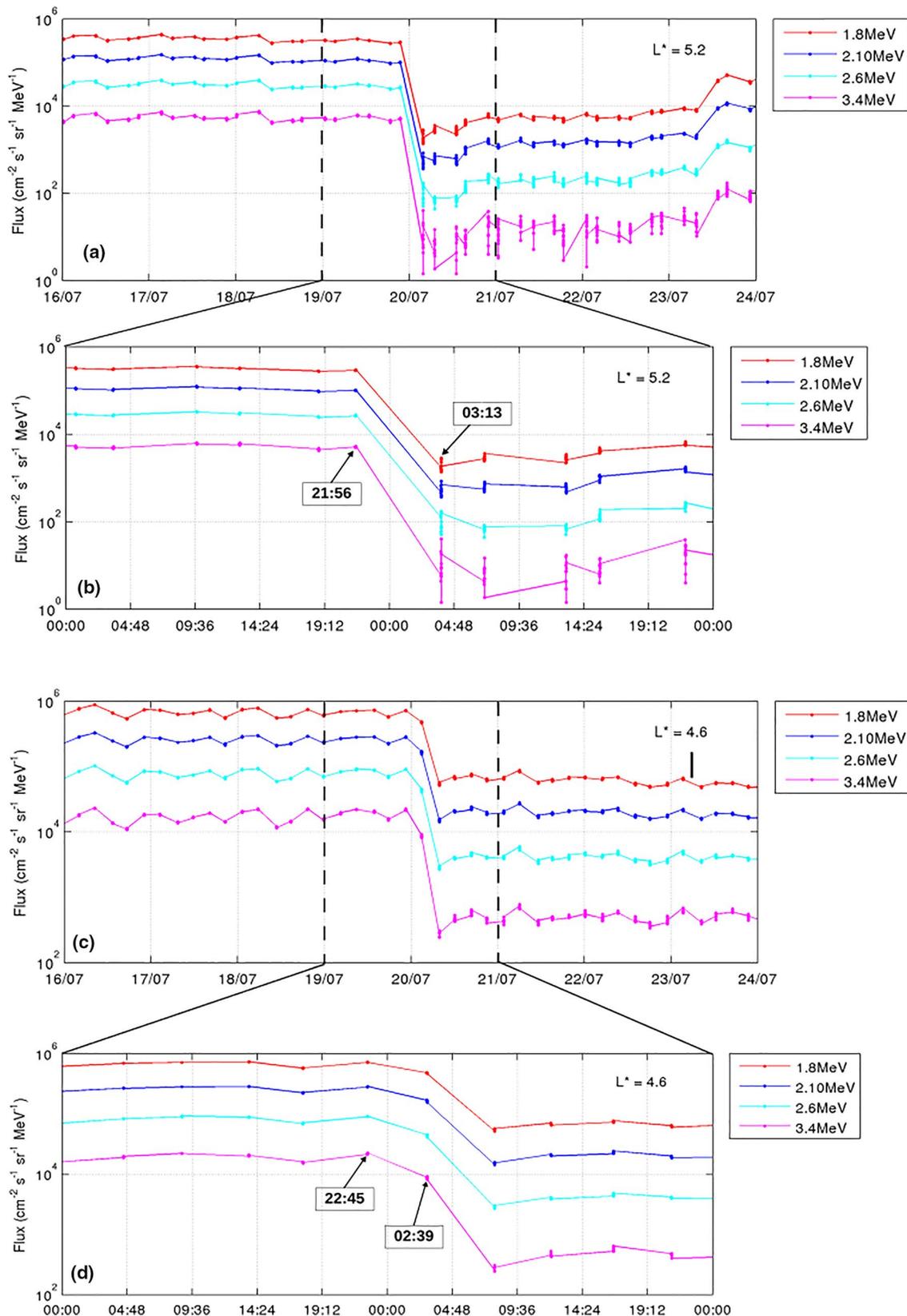
Figure 4. (a and b) electron fluxes at 1.8, 2.10, 2.6, and 3.4 MeV energies at a fixed $L^* = 5.2$ location. (c and d) same as panels (a and b) but at a fixed $L^* = 4.6$ location. The electron fluxes are obtained by the REPT instrument on board of the Van Allen Probes (B)
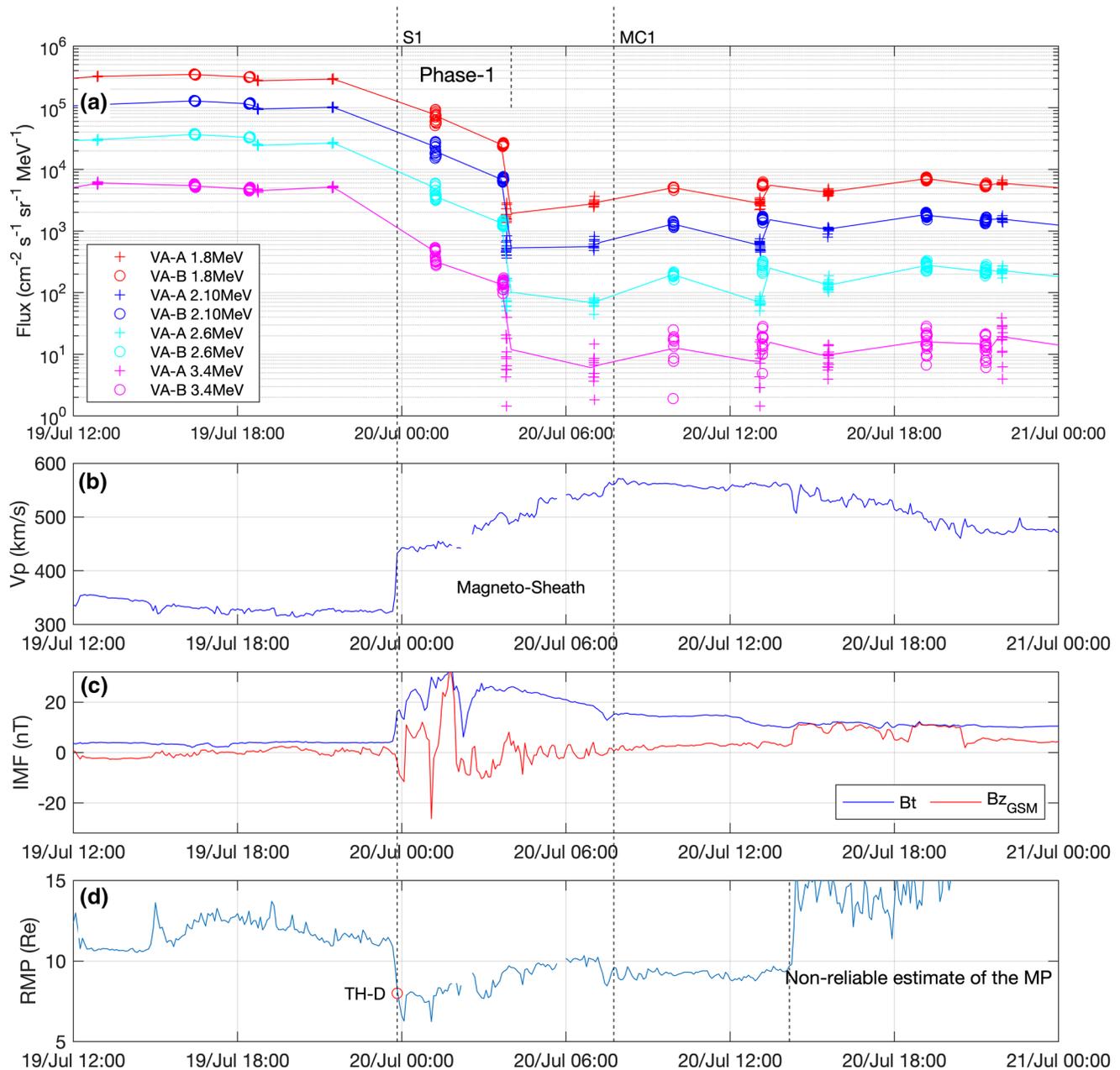
Figure 5. (a) electron fluxes at 1.8, 2.10, 2.6, and 3.4 MeV energies at a fixed $L^* = 5.2$ location; (b) solar wind speed (Vp); (c) Interplanetary Magnetic Field (IMF) intensity (Bt) and Bz component of the IMF; (d) Magnetopause stand-off distance by the Shue et al. (1998) model. The electron fluxes are obtained by the REPT instrument on board of the Van Allen Probes A and (b) The Vp, Bt, Bz, Bx, and By are obtained by the ACE satellite in the Lagrangian L1 point. TH-D represents the spacecraft THEMIS-D crossing magnetopause at ~23:50 UT (x-GSE ~8RE).

Geocentric Solar Magnetospheric (GSM) coordinate system. SWMF/BATS-R-US employs a Cartesian grid whose spatial resolution increases by factors of two as one approaches the Earth. Far downstream in the solar wind region the coarsest grid resolution used in our setup is 4 RE, whereas the finest grid resolution of 0.25 RE is used in a box surrounding Earth with dimensions $-7 \leq x,y \leq 7$ RE, and $-3 \leq z \leq 3$ RE. The inner boundary of SWMF/BATS-R-US is delimited by a sphere with 2.5 RE radius centered at Earth. Over this surface, the uniform temperature and plasma density number are specified at 25,000 K and at 28 cm^{-3}, respectively.
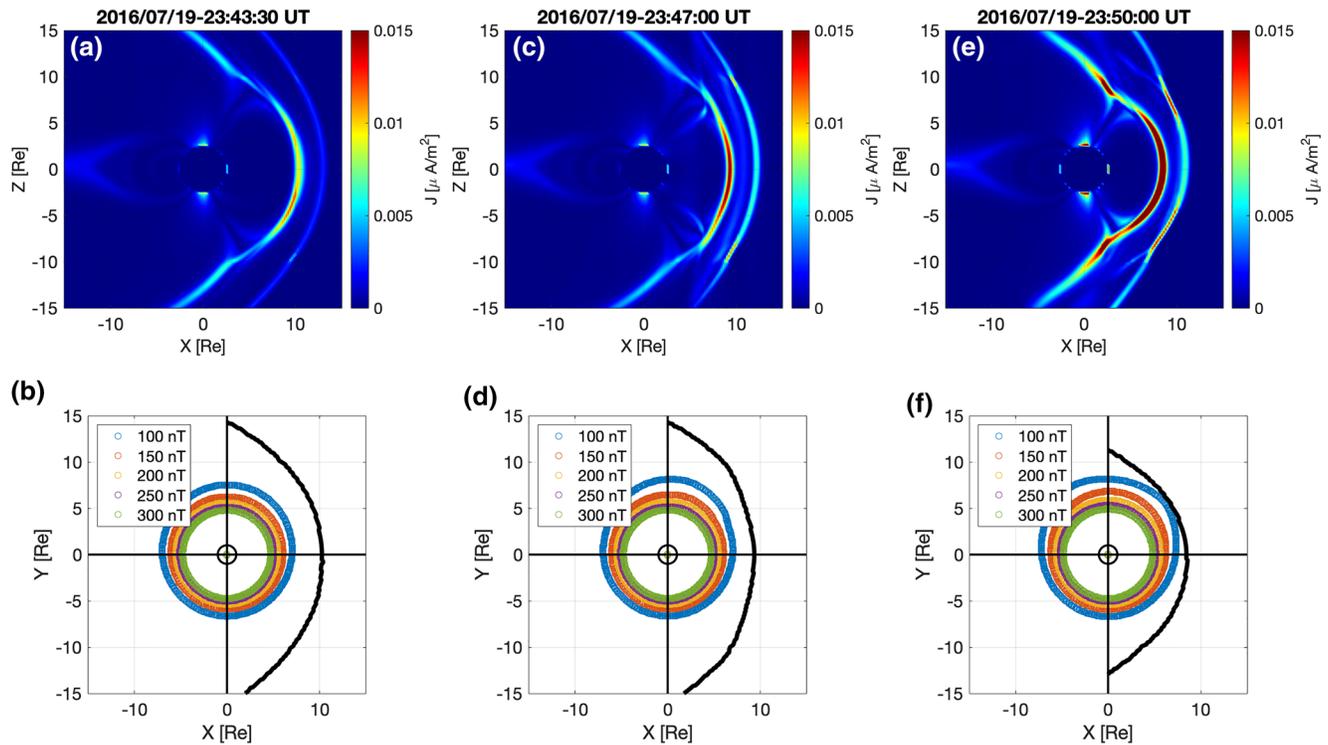
Figure 6. Global (MHD) simulation of the Earth's magnetosphere on the arrival of the ICME on July 19, 2016, considering the time-lagged by 45 min. Panels (a, c, and e) show instantaneous images of magnetospheric current density magn itude values in units of μA/m² (color's scale) extracted from the SWMF/BATS-R-US coupled with the RCM model at the X-Z GSM meridional plane. Panels (b, d, and f) show equatorial (X-Y GSM) cuts of the modeled magnetosphere at these instants of time. Color-coded lines in panels (b, d, and f) indicate magnetic field strength isocontours for different intensities (100 up to 300 nT). The black line on those panels represents the magnetopause stand-off distance in the dayside equatorial region. Panels (a–f) are referent to the global (MHD) simulation of the Earth's magnetosphere at 23:43:30 UT (prior to the ICME arrival), 23:47:00 UT (at the ICME arrival), and 23:50:00 UT (during the maximum magnetosphere compression), respectively. ICME, interplanetary counterpart of a solar coronal mass ejection.

Figure 6 presents the global MHD simulation results, considering the time-lagged by 45 min. Panels (a), (c) and (e) showing instantaneous images, at the X-Z GSM meridional plane, of the modeled magnetospheric current density magnitude values (in units of μA/m²) extracted from SWMF/BATS-R-US which has been coupled to the Rice Convection Model (De Zeeuw et al., 2004; Toffoleto et al., 2003). The domain of the RCM model is centered at Earth and extends up to about 7 RE–8 RE in the geocentric distance. The RCM model provides a self-consistent description of the electrodynamics of the coupled inner magnetosphere-iono-sphere system (see De Zeeuw et al., 2004, for an in-depth view of the RCM coupling with the global mag-netosphere module of SWMF/BATS-R-US). Briefly, RCM calculates a more accurate inner magnetosphere thermal plasma pressure by including the transport of the inner plasma sheet and ring current particles via gradient/curvature drifts. Such plasma pressure is then mapped back to the global magnetosphere module of SWMF/BATS-R- US. Panels (b), (d), and (f) show equatorial (X-Y GSM) cuts of the modeled magneto-sphere at time instants showed on top of the panels (a), (c), and (e), respectively. Such time instants refer to simulated magnetosphere parameters taken (a, b) prior to the ICME arrival, (c, d) at the ICME arrival, and (e, f) during the maximum magnetosphere compression. Color-coded lines in panels (b), (d), and (f) indicate magnetic field strength isocontours ranging from 100 (blue) up to 300 nT (green). They nearly cor-respond to drift paths of equatorially mirroring (i.e., nearly 90° equatorial pitch angle) electrons (see, e.g., Sibeck et al., 1987, for details). The black line in panels (b), (d), and (f) represents the equatorial, dayside magnetopause boundary which has been obtained by taking the maximum along radial profiles of the cur-rent density magnitude. During the maximum magnetosphere compression (panel e and f), the modeled magnetopause boundary intercepts the 100 nT isocontour line, which would correspond to the drift paths of equatorially mirroring electrons near geosynchronous orbit. Thus, such electrons would be lost to the adjacent magnetosheath region upon interception with the magnetopause (see also Medeiros et al., 2019),

therefore strongly suggesting that magnetopause shadowing significantly contributed to remove relativistic electrons from the outermost region of the outer Van Allen belt. We thus identify magnetopause shadowing as the first dynamical mechanism contributing to the high-energy electron loss during the turbulent ICME's sheath region.

4.2. Wave-Particle Interactions

Generally, during magnetically active periods, a number of electromagnetic waves can be excited and subsequently interact with radiation belt electrons, resulting in violation of one, two or even all three adiabatic invariants. ULF waves can violate the third adiabatic invariant and cause radial diffusion (Da Silva et al., 2019; Perry et al., 2005). Chorus waves and EMIC waves can violate the first and second adiabatic invariants, leading to both diffusive transport and advective transport to the loss cone (Horne & Thorne, 1998; Shprits, 2009). It is important to highlight that this case study occurred under the influence of an ICME and its turbulent sheath region. Even though this solar wind structure did not cause a strong geomagnetic storm, it may have excited electromagnetic waves in the magnetosphere. Therefore, first we need to detect the wave activities, and after that, we should carefully investigate the possibility of occurrence of the wave-particle interactions during the electron flux variability in the outer Van Allen radiation belt.

4.2.1. Outward Radial Diffusion by ULF Waves

ULF waves are generally excited at the magnetopause boundary in response to velocity shears (Claudepierre et al., 2008; Elkington et al., 2006) or to solar wind pressure fluctuations (Claudepierre et al., 2009; Ukhorskiy et al., 2006). They may also be excited internal to the magnetosphere by natural instabilities of the magnetospheric plasma (Elkington, 2006; Hasegawa, 1969; Southwood et al. 1969; Takahashi et al., 1985). Their properties can be obtained from both observational data and global MHD simulations, which in turn can be used to study the dynamic response of the outer belt electron flux to the solar wind variability (Fei et al., 2006; Kress et al., 2007).

ULF wave characteristics are used to evaluate the radial diffusion mechanism (Brautigam et al., 2005; Da Silva et al., 2019; Huang et al., 2010; Ozeke et al., 2014; Ukhorskiy et al., 2005). Observational ground-based data from the IMAGE network are used here to calculate ULF power spectral density (PSD) in the 1–8.33 mHz, that is., within the Pc5 frequency range, from July 16th to July 23rd, as shown in Figure 7 (upper panel). Notice that enhanced ULF wave activity started approximately at 23:00 UT on the 19th of July, which is almost coincident with the shock associated with the ICME (23:05 UT, see Figure 1). The ULF wave activity was as intense as 10^4 nT^2/Hz and sustained from 23:00 UT on the 19th until 04:00 UT on the 20th. The wave activities encompass most of the outer radiation belt at L-shell ≥3 during this specific time interval, which occurs under the influence of the ICME's sheath. The persistence, as seen by ground-based observatories, in ULF wave activity continued until approximately 18:00 UT on the 20th, meaning that the ULF waves were present in both ICME's sheath and magnetic cloud regions, and ULF waves were also observed after the magnetic cloud. Although the ULF waves have been detected outside the ICME's sheath, the electron flux dropout is not observed in this period.

Although the Van Allen Probe A location for this event to be near apogee between 00:00 and 01:30 UT, we would like a global vision of the ULF wave activities just after the strong ICME's sheath compression in the magnetopause. Therefore, we decided to use a global MHD model to simulate the ULF PSD in the inner magnetosphere at different MLT when the Earth's magnetosphere was influenced by the ICME and its turbulent sheath. Magnetohydrodynamic model is an essential tool to study space plasmas. It is extensively used by the scientific community to study the large-scale interaction between different solar wind structures and Earth's magnetosphere. It also has been widely used to address the low-frequency waves generation (in a few to tens of mHz range) like the ULF waves in the inner magnetosphere, specifically in the radiation belts (e.g., Alves et al., 2016; Claudepierre et al., 2010, 2008; Da Silva et al., 2019; Jauer et al., 2019; Komar et al., 2017; Souza et al., 2017). Da Silva et al. (2019) and Souza et al. (2017) used the SWMF/BATS-R-US model to study the ULF waves in the equatorial and nightside magnetosphere during the influence of the Alfvénic fluctuations associated with HSS. Claudepierre et al. (2008) used the Lyon-Fedder-Mobarry (LFM)
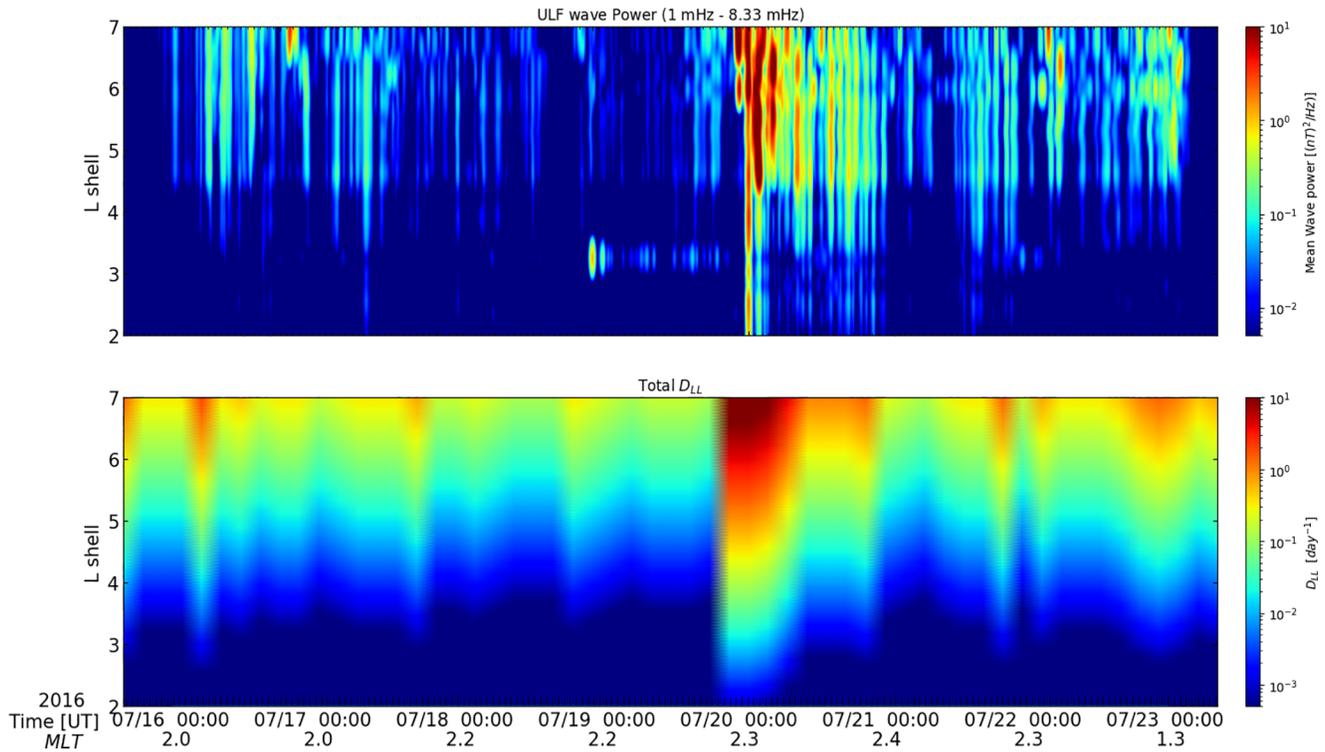
Figure 7. (top) IMAGE network's ULF power spectral density in the 1–8.33 mHz frequency range (color's scale) as a function of L-shell and time from July 16 to 22, 2016. (bottom) radial diffusion coefficient D_{LL} in units of day^{-1} (color's scale) as a function of L-shell (vertical axis) and time (horizontal axis from July 16–22, 2016), estimated from the Kp index data from the OMNI database with the help of the analytic expression derived by Ozeke et al. (2014). ULF, ultralow frequency.

model to study the production of ULF waves in the magnetosphere to the HSS. Both the results showed that the magnetopause motions in the flank regions are consistent with the Kelvin-Helmholtz (KH) instability, which drove the ULF waves in the inner magnetosphere.

Figure 8 shows the ULF PSD as a function of frequency and L-shell at noon, that is, at 12:00 MLT, simulated by the SWMF/BATS-R-US/RCM model on July 20, 2016 (00:30 to 01:00) (Figure 8-top), July 20, 2016 (01:00 to 01:30) (Figure 8-middle) and (01:30 to 02:00) (Figure 8-bottom). The 12:00 MLT analyses are discussed here to highlight the outward radial diffusion mechanism driven by ULF waves during the electron flux dropout, which coincides with the magnetopause shadowing mechanism. The parallel magnetic component (B||), azimuthal electric component (Eφ), and radial electric component (Er) are shown in the first, second, and third columns, respectively. The dipole inclination is not considered in this MHD simulation, and the radial distance analyses here are less than geosynchronous orbit. It means the magnetic equator is localized at the Z_GSM = 0, and the simulated magnetic field can be approximately considered as a purely dipolar field. Thereby, L* and L-shell are practically equivalent, as viewed in Figure 8.

ULF polarization modes were simulated for 00:00 MLT, 06:00 MLT, 12:00 MLT, and 18:00 MLT, to determine which ULF waves were significant in each MLT. Figure 8 presents the PSD at 12:00 MLT because it is important to verify the generation of the ULF associated with the arrival of the ICME at the Earth's magnetosphere. Compressional modes (B$_{||}$) just after the ICME arrival (Figure 8a) have a strong signature concentrated between L-shell = 3–5. During the next subsequent period (Figure 8b), B$_{||}$ presents signatures between L-shell = 3–6, followed (Figure 8c) by concentration between L-shell = 4–5. Poloidal mode (E$_{\varphi}$) and toroidal mode (E$_r$) electric fields were significant during all periods analyzed here. The simulation results show that the ULF waves may have contributed to the decrease in electron flux observed in the outer radiation belt, considering that the power of B|| and Eφ were considerably strong during all the time when the Earth's magnetosphere has been under the influence of the ICME's sheath.
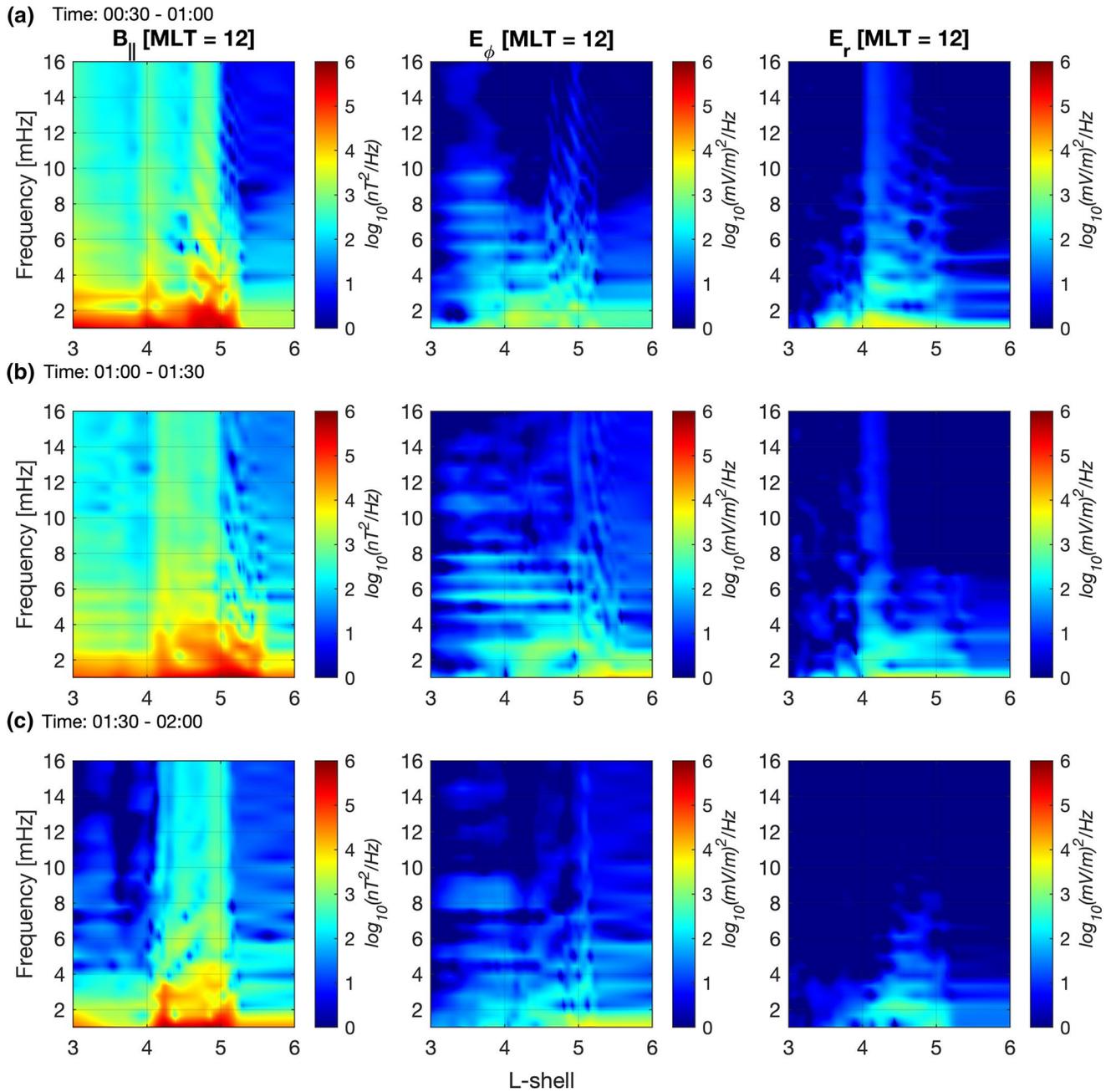
Figure 8. The ULF power spectral density (color's scale) as a function of frequency (vertical axis) and L-shell (horizontal axis) at 12:00 MLT simulated by the SWMF/BATS-R-US/RCM model on July 20, 2016 (a) from 00:30 to 01:00 UT, (b) from 01:00 to 01:30 UT, and (c) from 01:30 to 02:00 UT. The parallel magnetic component (B$_∥$), azimuthal electric field component (E$_φ$) and radial electric field component (E$_r$) are showed in the first, second and third column, respectively. ULF, ultralow frequency.

The ULF wave-particle interactions through drift resonances violate the third adiabatic invariant and enhance the outward radial diffusion. Radial diffusion can be estimated by an analytical expression derived by Ozeke et al. (2014). Then, the influence of the ULF waves in the high-energy electron flux dropout can be analyzed. Figure 7 shows (top) the ground-based ULF PSD in the 1–8.33 mHz frequency range, and (bottom) the radial diffusion coefficient D$_{LL}$ from July 16–22, 2016. D$_{LL}$, which is the sum of $D_{LL}^E + D_{LL}^B$ is estimated from the Kp index (OMNI database) according to Equations 8 and 9 of Da Silva et al. (2019), and intensifies when the shock reaches the Earth's magnetosphere. This intensity remains for approximately 4 h

during the influence of the ICME's sheath, which is concomitant with the beginning of ULF wave activities recorded in ground-based data. After that, D_{LL} presents a slight decrease that persists for approximately 4 h, and the second decrease during the influence of the ICME's magnetic cloud, which is coincident with ULF PSD calculated from ground-based data. Thereby, it is suggested that the outward radial diffusion mechanism contributed to the high-energy electron flux dropout observed during the influence of the ICME's sheath, since the D_{LL} is considerably significant in this region.

The identification of the dominant dynamic mechanism during the relativistic electron flux dropout is not straightforward since several mechanisms are detected at the same time. Therefore, it is important to investigate the influence of some magnetospheric waves during losses of radiation belt electrons via wave-particle interactions, in which we also include the investigations referent to the whistler-mode chorus and EMIC waves (see, Medeiros et al., 2019; Ni et al., 2013, 2015, 2017; Summers et al., 2007; Shprits, Kellerman, et al., 2017; Thorne, 2010; Turner et al., 2014) as discussed in the next subsections.

4.2.2. Pitch Angle Scattering—EMIC Waves

EMIC waves are generated in the magnetosphere from anisotropic (T⊥/T∥>1) distributions of ring current ion populations (∼10–100 keV) (Cornwall, 1965; Horne & Thorne, 1993; Jordanova et al., 2012; Kennel & Petschek, 1966). EMIC waves are discrete electromagnetic emissions, which usually are separated into hydrogen (H+), helium (He+), and oxygen (O+) bands by their corresponding ion gyrofrequencies. Magnetospheric compressions, as observed in this case study, can lead to anisotropic distributions for ring current ions, which generate EMIC waves on the dayside magnetosphere (see e.g., Denton et al., 2002; McCollough et al., 2010).

EMIC waves can have an important role in the loss of relativistic electrons to the upper atmosphere (see e.g., Medeiros et al., 2019; Sandanger et al., 2007; Thorne & Kennel, 1971; Usanova et al., 2014; X. J. Zhang et al., 2016). The ion composition is decisive to define how the wave-particle interaction can occur. EMIC waves appear mostly left-hand polarized, in the Pc1-2 ULF frequency range, that is, from 0.1 to 5 Hz, and the wave amplitude varies from 0.1 nT to 10s of nT (Halford et al., 2016). The local ion composition has been assumed (see e.g., Summers & Thorne, 2003 and Medeiros et al., 2019) here to define the wave-particle interaction effectiveness as well as wave amplitude, time duration, frequency band, and particle energy. The minimum resonant energy can be inferred by the Equation 1 (see e.g., Kang et al., 2016; Summers & Thorne, 2003):

$$
\begin{aligned}
E_{min} &= \left[\left[1 - \left(v_{\parallel}^2 / c^2 \right) \right]^{-1/2} - 1 \right] m_e c^2 \\
&= \left[\left(1 - \beta_{\parallel}^2 \right)^{-1/2} - 1 \right] m_e c^2,
\end{aligned}
\tag{1}
$$

where,

$$
\beta_{\parallel} = \frac{v_{\parallel}}{c} = \frac{xy + |s| n \left(n^2 - x^2 + y^2 \right)^{1/2}}{\left(n^2 + y^2 \right)},
$$

$$
x = \frac{\omega}{|\Omega_e|}, \quad y = \frac{ck}{|\Omega_e|},
$$

$v_{\parallel}$ is the electron velocity parallel to the field line, m_e is the electron rest mass, ω and k are the angular frequency and wave number of EMIC waves, respectively, Ω_e is the electron gyrofrequency, c is the speed of light, n is the resonance harmonic number (assumed to be 1), and finally s is set to be -1 for the left-hand mode.
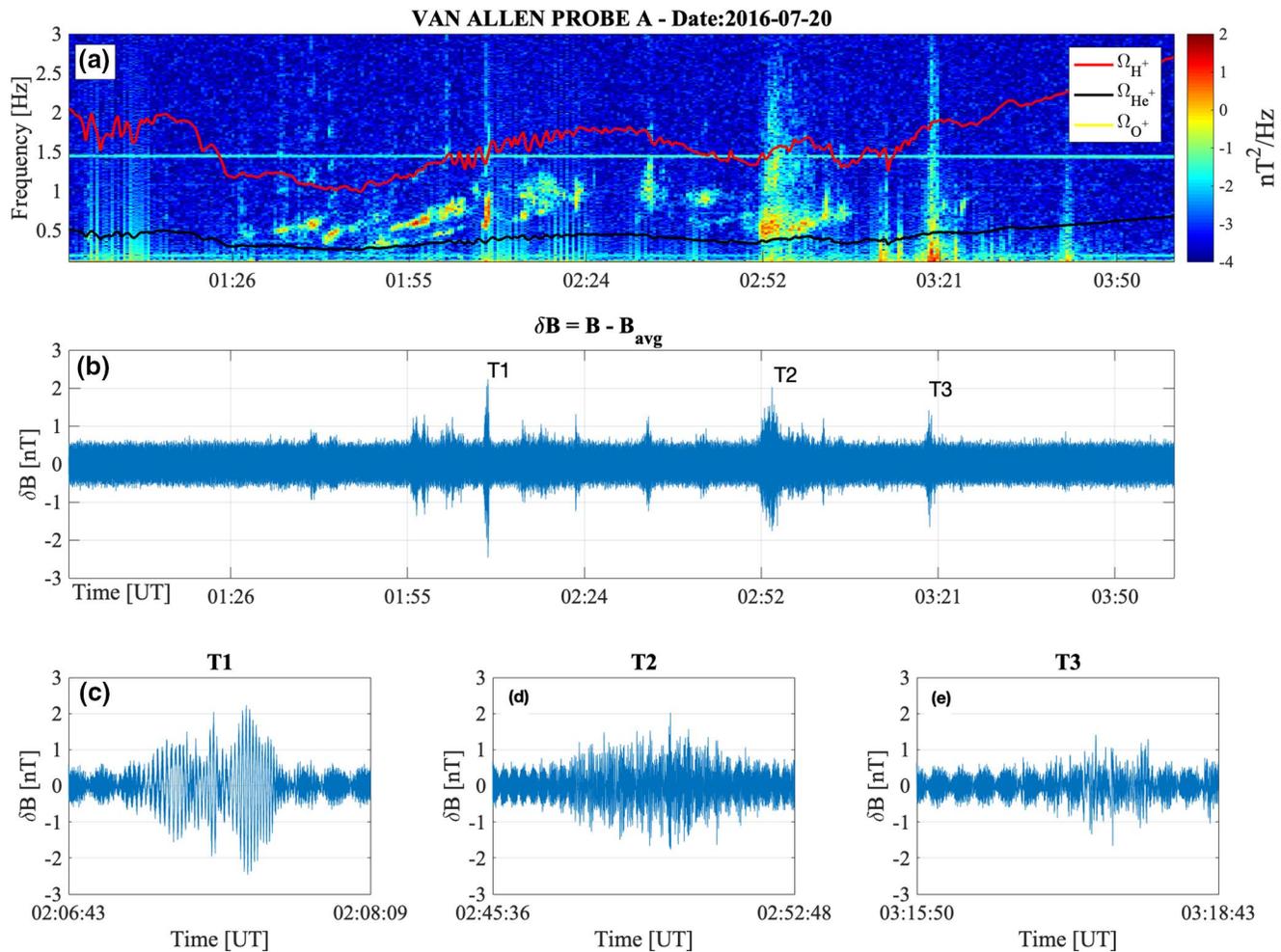
Figure 9. The EMIC power spectral density (color's scale) as a function of frequency (vertical axis) and time (horizontal axis) (top) and the magnetic field perturbation (middle) on July 20, 2016, at 1–4 UT. T1, T2, and T3 are three specific periods of EMIC wave activities (bottom). Data from the EMFISIS instrument on board Van Allen Probe A were used. EMFISIS, Electric and Magnetic Field Instrument Suite and Integrated Science; EMIC, electromagnetic ion cyclotron.

The literature (Halford et al., 2010; Meredith et al., 2014; Usanova et al., 2012) shows that the occurrence rate of EMIC waves can increase during geomagnetic storms, as well during nonstorm periods. The ICME detected by the ACE satellite (Figures 1c–1f) for this event exhibits a strong shock and a strong spike in the north-south component Bz, while the SYM-H index that reached +50 nT confirms the storm sudden commencement and the AE index that reached 1,000 nT confirms substorm activity, so it is important to investigate EMIC wave activities. Van Allen Probe B measurements were not propitious at the beginning of the ICME's sheath region, because the satellite was at perigee. Therefore, we use Van Allen Probe A measurements to analyze EMIC waves from approximately 01:00 UT on July 20, in which the EMIC activities are persistent for approximately 3 h (under the influence of the ICME's sheath). Figure 9 shows the EMIC PSD as a function of frequency and time (top) and the magnetic field perturbation δB, on July 20, 2016, from 01:00 UT to 04:00 UT (middle). T1, T2, and T3 are three specific periods of EMIC activities (bottom). EMIC PSD (Figure 9, top) shows a considerable time interval containing EMIC wave signatures in the Hydrogen band starting at 01:55 UT. The beginning of the EMIC wave activity almost coincides with the high-energy electron flux dropout in $L^* < 4.7$ (See Figure 4d). The T1 box shows a well-defined packet of EMIC waves with strong (a few nT) amplitudes in a short time period, which is used here to analyze their potential to interact with the high-energy electrons under the influence of the ICME's sheath.

EMIC wave-particle interactions through the gyroresonance violate the first and second adiabatic invariant and lead to pitch angle scattering and diffusive transport (e.g., Kennel & Petschek, 1966). The minimum resonance energy is calculated here using the most intense EMIC waves. In this context, we assumed the plasma composition to be H+ = 75%, He+ = 20% and O+ = 5% (see e.g., Medeiros et al., 2019; Summers & Thorne, 2003). We also consider cold plasma dispersion and take the frequency where the most intense wave packet occurs is 0.8 Ω_{H+}, where Ω_{H+} is the proton gyrofrequency. The spacecraft potential provides the electron number density and the minimum resonance energy calculated is 1.2 MeV, which indicates that the EMIC wave packets observed in this event can resonantly interact with electrons ≥1.2 MeV. Consequently, EMIC waves may have scattered electrons to the loss cone (see e.g., Medeiros et al., 2019) during the high-energy electron flux dropout in the outer radiation belt under the influence of the ICME's sheath.

4.2.3. Pitch Angle Scattering—Chorus Waves

Whistler-mode chorus waves are intense natural plasma waves that occur in the Earth's magnetosphere (Helliwell, 1969; Storey, 1953). Their signatures are usually observed in the region outside the plasmapause (Burton & Holzer, 1974; Lauben et al., 2002; LeDocq et al., 1998). Chorus waves typically occur over a wide frequency range from hundreds of Hz up to about 10 kHz (Gurnett & O'Brien, 1964) generated by the electron cyclotron instability near the equator (Agapitov et al., 2012, 2013; LeDocq et al., 1998) in association with injected plasma sheet electrons (Kennel & Petschek, 1966). Chorus wave activity intensifies during enhanced substorm activity and also during the recovery phase of geomagnetic storms (Agapitov et al., 2015, 2018; Meredith et al., 2001).

Chorus waves generally occur in two distinct bands above and below half of the electron gyrofrequency (Tsurutani & Smith, 1974), and they are termed as upper and lower band and chorus, respectively. Wave-particle interactions mediated by lower band (LB) chorus play an important role in the loss of radiation belt electrons (Bortnik & Thorne, 2007; Horne & Thorne, 1998; Thorne et al., 2010), in which the scattering processes can occur and the energetic particles can be lost to the atmosphere as diffuse auroral precipitation (W. Li et al., 2014; Ni et al., 2008; Nishimura et al., 2010, 2011; Thorne et al., 2010). The scattering processes here are investigated analytically under the quasilinear approximation (Mourenas et al., 2014) during the flux decrease observed at $L^* \leq 4.6$ (~01:55:30 UT to 02:00:00 UT on July 20, 2016) (See Figure 4d).

Figure 10 shows the magnetic field dynamic power spectrum from the EMFISIS instruments aboard Van Allen Probes A (panel a) and B (panel c) measured at $L^* \sim 4$–5 and magnetic latitude $\lambda \sim 2°$ for a 6-h period (00:00 UT to 06:00 UT on July 20, 2016), under the influence of the ICME's sheath. Panels (b) and (d) present the whistler wave normal angle for this time interval. The structure of chorus waves is presented in panels (e) which shows the wave form and (f) the dynamic spectrum. The structured rising tone elements are observed in the frequency range from 0.2 f_{ce} to 0.4 f_{ce}. The average wave amplitudes are about 200 pT (with maximal values up to 1–2 nT). The observed wave amplitude lead to significant pitch-angle scattering with characteristic scales of about an hour for 1 MeV electrons. Taking into account the obliqueness of the observed waves the scattering time scales for these amplitudes can be 2–3 times less, that is, about tens of minutes leading to significant decrease of the core population of the outer radiation belt (Artemyev et al., 2013, 2016). The high geomagnetic activity level (the AE index exceeded 800 nT) can lead to decrease of ω_{pe}/Ω_{ce} ratio especially in the night sector of the outer radiation belt providing additional efficiency to wave-particle interactions (O. Agapitov et al., 2019). Therefore, we can suggest that pitch angle scattering by chorus wave-particle interaction may have contributed to high-energy electron flux dropout observed in the outer radiation belt under the influence of the ICME's sheath from 01:55 UT on 20 July.

During the chorus wave activities during the ICME's sheath there are also some local enhancements of flux at $L^* \sim 3.5$–4.5 due to the observed field-aligned waves (Figure S1). Therefore, it is worth noting that sometimes chorus wave-particle interaction also may have contributed to the acceleration of particles during the turbulent ICME's sheath region, especially when field-aligned chorus waves are observed. Additionally, although the chorus wave activities also occur during the magnetic cloud region (Figure S1), and the predominance of the obliqueness of this observed waves persist several hours, the high-energy electron flux dropout during the magnetic cloud is subtle, that is, the flux decreases by less than one order of magnitude.
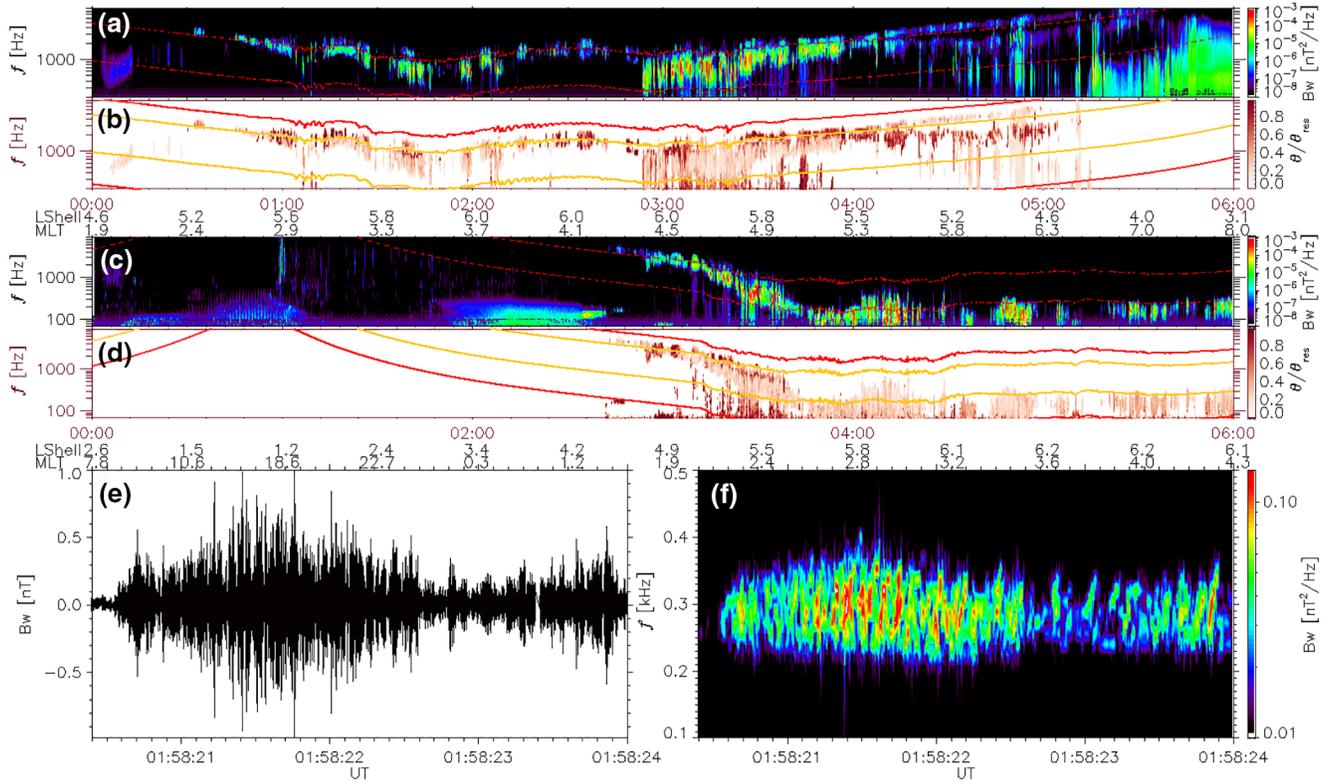
Figure 10. Magnetic field dynamic spectra and the wave normal angle as a ratio of wave normal angle θ on θ_{res} ($\cos \theta_{\text{res}} = \omega/\Omega$) from the Van Allen A (a and b) and B (c and d). The waveform (e) and high-resolution dynamic spectra (f) show the chorus emission structure with rising tone elements.

Similar results during the influence of the ICME's sheath region are obtained making use of the interaction of relativistic electrons with several chorus subelements (e.g., Alves et al., 2016). Figure 11 presents in panel (a) magnetic field spectrograms for EMFISIS measured at $L^* \sim 5$ and magnetic latitude of $\sim 0.5°$ for a 5-h period going from 00:00 UT to 05:00 UT on July 20, 2016, and in panel (b) a zoom-in of the data shown in panel (a) with a 4.5 min period going from 01:55:30 UT to 02:00:00 UT also on July 20, 2016. The arrows in Figure 11b indicate when burst mode data were available for the selected period. The selected chorus subelement (Figure 11c) presented the wave magnetic field amplitude $B_{\max} \geq 0.5$ nT. Panel (c) shows the high-resolution magnetic field measurements correspond to a period of higher magnetic spectral density as shown in panel (b).

Several chorus subelements were identified during the intervals where burst mode data were available, and an example of a chorus subelement is shown in Figure 11c. For three of such subelements taken at times 01:57 UT, 01:58 UT and 01:59 UT indicated by the red arrows in Figure 11b, we compute the change in pitch angle according to Equation 2 below undergone by an electron as a result of the cyclotron resonant interaction with the chorus wave for the whole subelement period τ, as well with only one wave cycle period T. Each period duration is illustrated in Figure 11c.

$$\Delta \alpha_i = \frac{B_{\max}}{B_0} \frac{\Omega_e}{\gamma} \Delta t_i \qquad (2)$$

where $B_{\max}$ is the peak instantaneous wave packet amplitude, B_0 the equatorial ambient magnetic field magnitude, Ω_e the electron cyclotron frequency, γ the Lorentz factor, and $\Delta t_i = i V_g / V_s$ (Lakhina et al., 2010). The term Δt_i is the ratio between the chorus subelement's scale size $i V_g$, where i can be either τ (subelement's time duration) or T (corresponding to one wave cycle period) and V_s. V_g is the group velocity and V_s is the relativistic relative velocity between the chorus wave and the electron's parallel resonant velocity calculated in the satellite frame. From Figure 11c, the parameters used in Equation 2 are identified as follows:
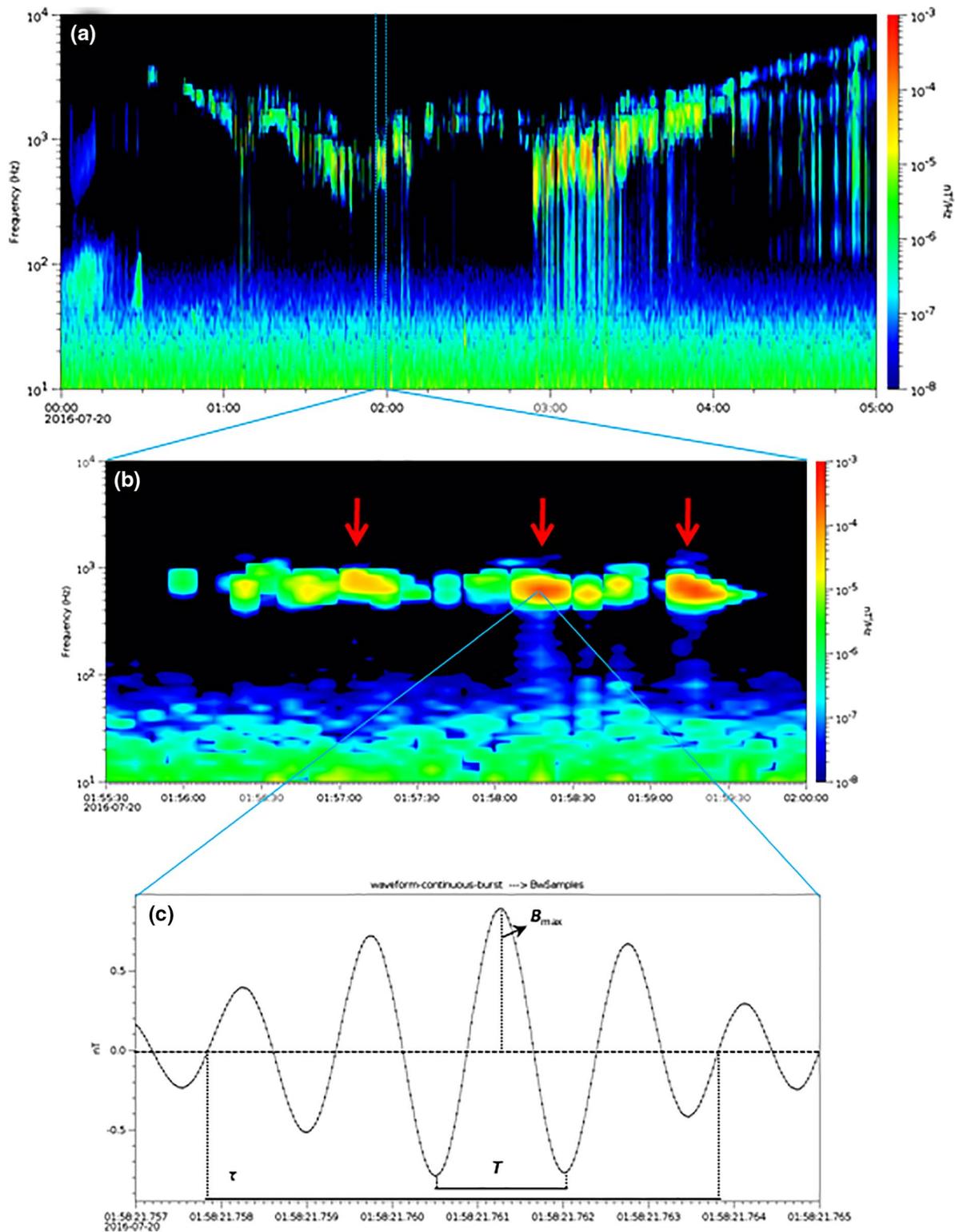
Figure 11. (a) EMFISIS' magnetic field spectrogram measured at $L^*\sim5$ and magnetic latitude $\sim0.5°$ for a 5-h period (00:00 UT to 05:00 UT July 20, 2016). (b) EMFISIS' magnetic field spectrogram measured at $L^*\sim5$ and magnetic latitude $\sim0.5°$ for a 4.5 min period (01:55:30 UT to 02:00:00 UT July 20, 2016). Arrows indicate when burst mode data were available for the selected period. (c) The high-resolution magnetic field measurements corresponding to a period of higher magnetic spectral density. Several chorus subelements were identified during the signature of the burst mode data as seen in panel (b), and panel (c) shows an example of it. Relevant parameters used in Equation 2 are identified as follows: B_{max}, the maximum instantaneous absolute value of the wave amplitude, T corresponding to one wave cycle period, and τ the subelement's time duration. EMFISIS, Electric and Magnetic Field Instrument Suite and Integrated Science.

Table 1
Parameters Used in 2 for Three Different Time Chorus Subelements

Time chorus subelements	τ(ms)	T (ms)	B_{max} (nT)	f_{pe}/f_{ce}	V_{ph} (m/s)	V_g (m/s)	Δt_τ(ms)	Δt_T (ms)	$\Delta\alpha_\tau$(°)	$\Delta\alpha_T$ (°)
01:57:15:945 UT–01:57:15:951 UT	6.0	1.5	0.64	6.08	2.82E + 07	5.63E + 07	32.32	8.08	46.09	11.52
01:58:21:757 UT–01:58:21:763 UT	6.0	1.5	0.90	6.37	2.55E + 07	5.10E + 07	30.93	7.73	62.02	15.51
01:59:17:957.1 UT–01:59:17:964.5 UT	7.4	1.5	0.73	5.81	2.74E + 07	5.47E + 07	37.98	7.60	70.23	14.05

$B_{max} = \sim 0.9$ nT, the maximum instantaneous absolute value of the wave amplitude, $T = 1.5$ milliseconds corresponding to one wave cycle period and $\tau = 6.0$ ms the subelement's time duration.

According to the description above, Table 1 shows the parameters obtained directly from the observational data, as τ, T, B_{max}, B_0, and n (electron density), and the derived parameters as f_{ce} (electron cyclotron frequency), f_{pe} (electron plasma frequency), V_{ph} (phase velocity), V_g, Δt_τ, Δt_T, $\Delta\alpha_\tau$, and $\Delta\alpha_T$. We chose one subelement for each of the following times 01:57:15:945 UT–01:57:15:951 UT, 01:58:21:757 UT–01:58:21:763 UT and 01:59:17:957.1 UT–01:59:17:964.5 UT to compare the characteristics of the parameters observed. The ratio f_{pe}/f_{ce} was above 5 during each of these three chorus subelements. According to Horne et al. (2003), this means that the chorus wave activities detected during each subelement here are not favorable to any acceleration process.

The three chorus subelements had similar characteristics. Each τ had approximately 4.0–5.0 wave cycles T (see Figure 11c), that is, $\tau \sim 4.5$ T during this electron flux dropout observed in the outer radiation belt. Considering the longer interaction time between an electron and a chorus subelement to be four/five wave cycle periods, the estimated change in pitch angle $\Delta\alpha_\tau$ is between 46.09° and 70.23°. Considering the shorter interaction time between the electron and chorus subelements to be one wave cycle period, the estimated change in pitch angle $\Delta\alpha_T$ was considerably lower than $\Delta\alpha_\tau$, namely, between 11.52° and 15.51°. In this way, from the analysis of the chorus subelements, we can also suggest that the pitch angle scattering via wave-particle interaction mediated by whistler mode chorus waves may have contributed to the electron flux dropout observed under the influence of the ICME's sheath.

5. Discussion

The decrease of relativistic electron flux in the outer radiation belt occurred during a storm sudden commencement period, under the influence of an ICME and its turbulent sheath. The main dynamic mechanisms related to this high-energy electron flux dropout were described in the previous section, in which we considered the influences of the wave-particle interaction and magnetopause compressions. Thereby, to discuss and confirm each mechanism identified before, the present section presents the analyses of the pitch angle distribution (PAD) and the time evolution of radial profiles of phase space density (PhSD).

5.1. Pitch Angle Distribution Analyses

PADs provide essential information concerning the physical processes taking place at or prior to the time of the measurement, either remotely or locally (Horne et al., 2003; Sibeck et al., 1987; Souza et al., 2018). Figure 12 show (from top to bottom) the electron PAD (vertical-axis) as a function of time (horizontal axis) for the 2.10 MeV energy channel (color's scale); the magnetic field dynamic spectra (color's scale) as a function of frequency (vertical axis), and time (horizontal axis) to EMIC, Chorus, and ULF waves, respectively, obtained from Van Allen Probe A for the period of July 19 at 22:30 UT to July 20 at 06:00 UT.

The PAD shows the high-energy flux dropout in the pitch angles between 50° and 130° in three periods. The first period occurred in approximately 30 min, starting at 00:45 UT, between the pitch angle 60° and 120°. The second dropout period persisted around by 1 h, between pitch angles 50° and 130°. In contrast, the third period of the dropout had a considerably shorter period of occurrence and pitch angle range, as it persisted a few minutes between the pitch angles 80° and 110°. The high-energy flux dropout observed
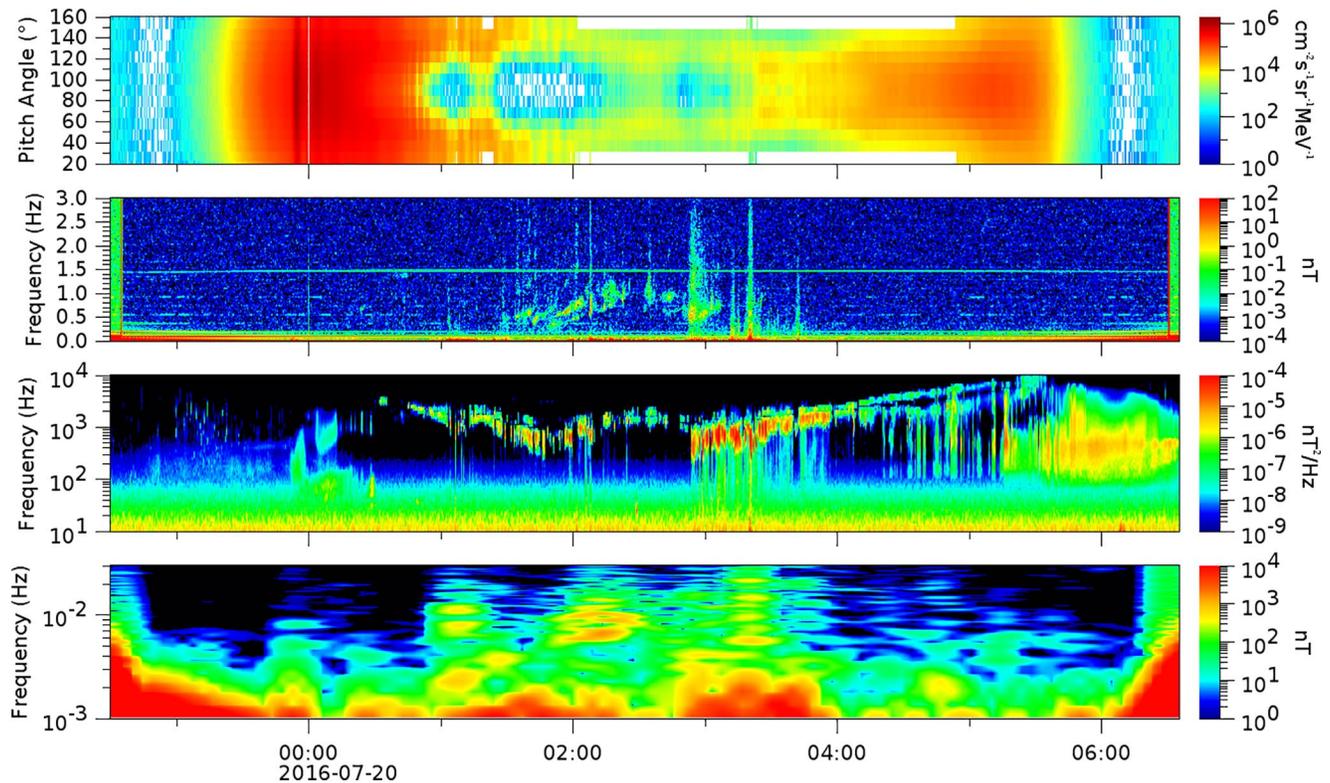
Figure 12. (From top to bottom) the electron PAD (vertical-axis) as a function of time (horizontal axis) for the 2.10 MeV energy channel (color's scale); the magnetic field dynamic spectra (color's scale) as a function of frequency (vertical axis), and time (horizontal axis) to EMIC, Chorus, and ULF waves, respectively. The data is obtained from Van Allen Probe A for the period of July 19 at 22:30 UT to July 20 at 06:00 UT. EMIC, electromagnetic ion cyclotron; ULF, ultralow frequency.

in the pitch angles between 50° and 130° to each period is concomitant with significant signatures of the ULF waves (Figure 12, bottom) between 1 and 10 mHz. The outward radial diffusion by ULF waves occurs through the drift resonance process (Schulz & Lanzerotti, 1974), in which the adiabatic transport of electrons can affect this drift resonance condition. It means that the radial transport rate will vary with each equatorial pitch angle. Thereby, the ULF waves' radial diffusion depended on the equatorial pitch angle (see Kamiya et al., 2018). It means the radial diffusion driven by ULF waves is responsible for these flux dropouts observed in the pitch angles between 50° and 130° (e.g., Alves et al., 2016; Ozeke et al., 2014; Ukhorskiy et al., 2005), as discussed in Section 4.2.1.

Besides the outward radial diffusion driven by ULF waves, the PAD morphology observed during the first dropout may have also been generated by the combination of the different mechanisms, as magnetopause shadowing (e.g., Baker et al., 2016; Kim et al., 2008) through the compression on the magnetopause discussed in Section 4.1, drift orbit bifurcation (e.g., Shabansky, 1971; Ukhorskiy et al., 2011, 2014), and drift shell splitting (e.g., Sibeck et al., 1987; Zheng et al., 2016). Here we discuss only the magnetopause shadowing. Occurrences of both drift orbit bifurcation and drift shell splitting are not necessarily associated with dropout events. So, as the focus here is to identify and understand the main dynamic mechanisms responsible by the high-energy electron flux dropouts in the outer belt, we concentrated and confirmed that both magnetopause shadowing and outward radial diffusion mechanisms contributed to this first dropout observed from 00:45 UT.

The high-energy flux dropout is also observed in the pitch angles between 130°–160° and 20°–50°. The first flux decrease for these pitch angles is considered moderate (approximately 1 order of the magnitude), observed around 01:00 UT and 01:45 UT. This period is concomitant with the whistler-mode chorus waves. Usually, the chorus waves are generated near the equator and propagate toward higher latitude. They

interact with bouncing, counter-streaming electrons in both hemispheres through the cyclotron resonance, launching the electrons into the loss cone (see Kasahara et al., 2018). It means that the pitch angle scattering driven by chorus waves is responsible for this first flux dropout observed in these pitch angles. The second flux dropout for these pitch angles is observed since 01:45 UT, persisting until approximately 04:00 UT, coincident with the EMIC wave life time. The EMIC waves are generally generated near the equator, in which its polarization turns linear as they are convected away from the magnetic equator. These Left-hand polarized EMIC waves resonate predominantly with low pitch angle relativistic electrons (see Summers et al., 2007). It is essential to highlight that the chorus waves also were present in this period. The PAD morphology observed here confirms that particles were lost to the atmosphere by pitch-angle scattering mechanism through the EMIC wave-particle interaction (see, Aseev et al., 2017 and Usanova et al., 2014) and chorus wave-particle interaction discussed at Sections 4.2.2. and 4.2.3, respectively.

5.2. PhSD Analysis

PhSD is an important tool to confirm the dynamic mechanisms related to high-energy electron flux decreasing on the outer radiation belt under the influence of the ICME and its turbulent sheath region. PhSD is calculated as a function of μ, K, and L* parameter, which are adiabatic invariants that constrain the electron motions. The first adiabatic invariant (μ) is dependent upon both the particle's pitch angle and the particle's energy. The second adiabatic invariant (K) depends upon the pitch angle. The inverse of the third adiabatic invariant (L*) depends upon both position and pitch angle (Green & Kivelson, 2004; Hartley et al., 2014; Schulz & Lanzerotti, 1974; Walt, 1994).

Conversion of the measured particle flux to PhSD for fixed invariants is obtained as follows (Hartley et al., 2014):

(1) PhSD is calculated from the Calculated K to local pitch angles (RBSP-A) available at https://www.rbsp-ect.lanl.gov/data_pub/rbspa/MagEphem/definitive/, which is obtained from the geomagnetic field model TS04 (Tsyganenko & Sitnov, 2005). We obtain α for a chosen K, that is, αK

(2) Equation 3 below is used to calculate μ and E for the pitch angle α_K, and obtain E$_\mu$

$$\mu = \frac{\left(E^2 + 2m_0c^2E\right)sin^2\alpha_K}{2m_0Bc^2}$$ (3)

(3) Obtain fluxes at α_K
(4) Obtain fluxes at E$_\mu$
(5) Equation 4 below is used to convert measured flux j to PhSD f

$$f\left(\mu,K,x,t\right) = \frac{j\left(\mu,K,x,t\right) * c^2}{\left(E^2 + 2m_0c^2E\right)}$$ (4)

(6) We use calculated L* values available at: https://www.rbsp-ect.lanl.gov/data_pub/rbspa/MagEphem/definitive/

(7) Finally, we obtain PhSD in adiabatic invariant coordinates

$$f\left(\mu,K,L^*,t\right)$$

The adiabatic invariants are conserved under specific circumstances (Roederer, 1970). PhSDs were calculated from RBSP-A data for values of μ = 1,000, 1,500, 2,000, and 2,500 MeV/G and K = 0.041 and 0.128 G$^{1/2}$R$_E$. These *K* values were chosen because they optimize the coverage of L* while limiting both the equatorial PhSD to approximately 70°–90° pitch angle range (K = 0.041 G$^{1/2}$R$_E$) (see Da Silva et al., 2019; Reeves et al., 2013; Souza et al., 2017), and the PhSD to approximately 50°–60° pitch angle range (K = 0.128 G$^{1/2}$R$_E$) (see Aseev et al., 2017; Iles et al., 2006; Shprits, Horne, et al., 2017). The μ values chosen (μ = 1,000, 1,500, 2,000, and 2500 MeV/G) correspond to electrons at relativistic energies (See, Boyd et al., 2016 and Murphy

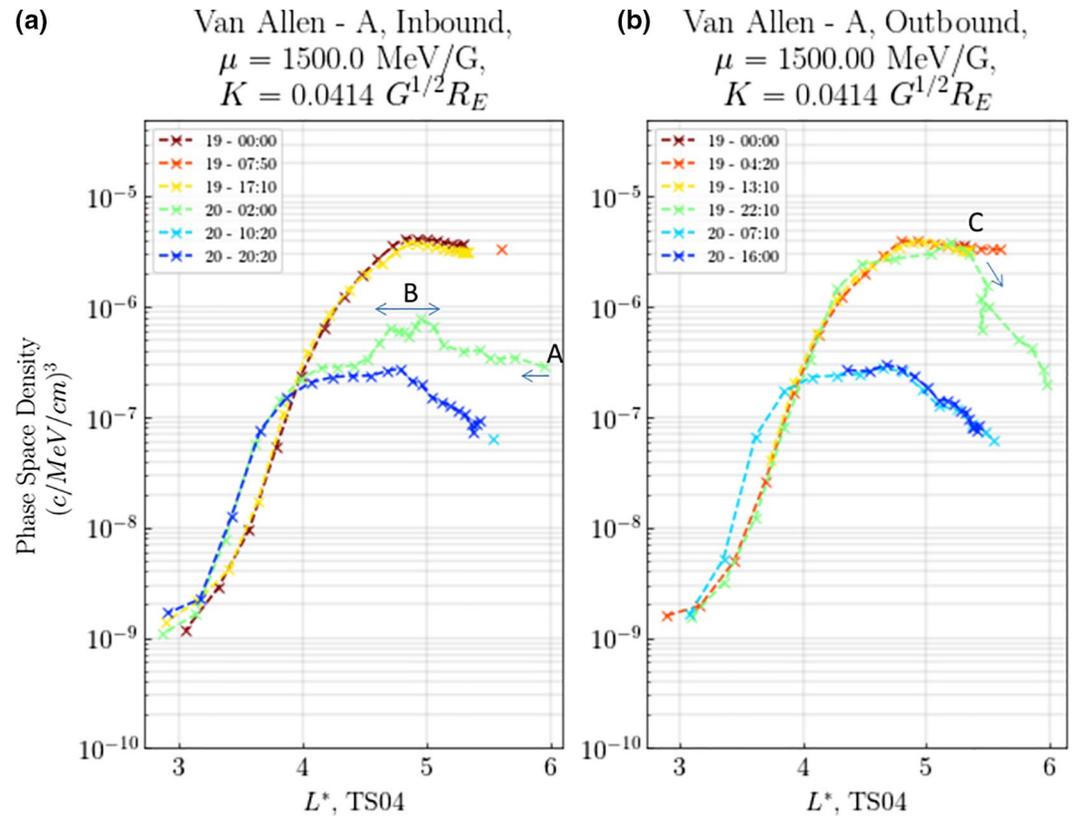**Figure 13.** Time evolution of phase space density radial profiles at fixed first ($\mu = 1500$ MeV/G) and second ($K = 0.041$ G$^{1/2}$R$_E$) adiabatic invariants for both (a) inbound and (b) outbound parts of the RBSP-A orbit. The inserts in Figures a and b show the start day and time (in the dd/hh:mm format) of either the inbound or outbound portions of RBSP-A.

et al., 2018) at which the decrease in the outer radiation belt flux is observed. Due to the behavior of the relativistic energies to be practically the same only the Figures referent to $\mu = 1500$ MeV/G (Figures 13 and 14) are shown here and the Figures referent to others μ values are shown in the Supporting Information (Figures S3–S8).

Figure 13 shows the time evolution of PhSD radial profiles as a function of L* for fixed first ($\mu = 1500$ MeV/G) and second ($K = 0.041$G1/2RE) adiabatic invariants for both (a) inbound and (b) outbound parts of the RB-SP-A orbits. The legend shows the start day and time in the dd/hh:mm format for both the inbound and outbound portions. The time evolution of the PhSD profiles in the inbound regions of the Van Allen Probes A orbit (Figure 13a) presents the flux decrease from L* = 4 (green curve—from 02:00 UT), highlighted by feature A. This profile confirms that the outward radial diffusion mechanism may have contributed to the high-energy flux dropout at such L* values (see Da Silva et al., 2019; Reeves et al., 2013; Souza et al., 2017). The outward radial diffusion mechanism observed here agrees with the results presented in Section 4.2.1. Feature B refers to a small peak that indicates local acceleration between L* ~4.5 and 5.2 (green curve). This local acceleration is probably driven by chorus wave-particle interaction, as discussed in Section 4.2.3. Figure 13b (outbound) presents a significant electron flux decrease from L* = 5.3 (green curve—from 22:00 UT), highlighted by feature C. This profile confirms that the magnetopause shadowing mechanism contributed to the high-energy electron flux dropout, as discussed in Section 4.1 (see Figure 16 by W. Li & Hudson, 2019). These results for $\mu = 1,500$ MeV/G are similar to $\mu = 1,000$, 2,000, and 2,500 MeV/G (see Figures S3–S5).

Figure 14 shows the time evolution of PhSD radial profiles as a function of L* for fixed first $\mu = 1,500$ MeV/G and second $K = 0.128$ G$^{1/2}$R$_E$ adiabatic invariants for both (a) inbound and (b) outbound parts of the RBSP-A.
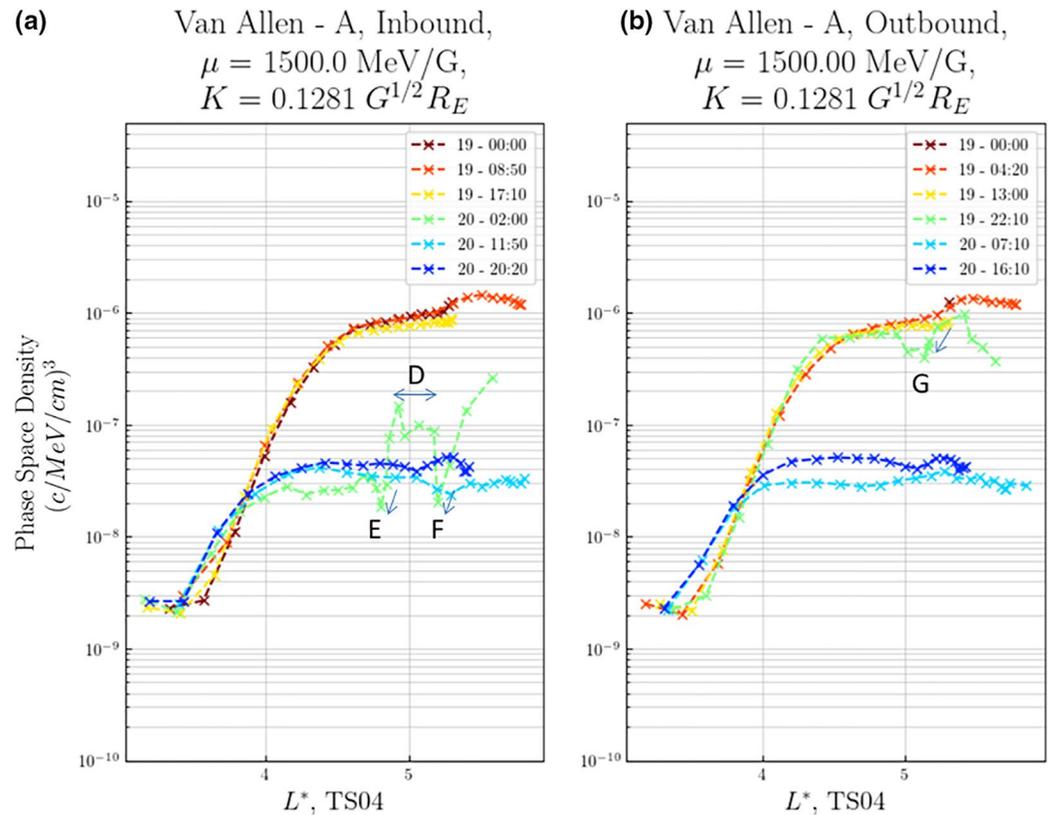
Figure 14. Time evolution of phase space density radial profiles at fixed first ($\mu = 1500$ MeV/G) and second ($K = 0.128$ G$^{1/2}$R$_E$) adiabatic invariants for both (a) inbound and (b) outbound parts of the RBSP-A orbit. The inserts in Figures a and b show the start day and time (in the dd/hh:mm format) of either the inbound or outbound portions of RBSP-A.

Figure 14a presents the time evolution of the PhSD profiles in the inbound regions of the Van Allen Probes A orbit, in which two local flux decreases (green curve—from 02:00 UT) are observed, the first in L* ~4.8 (feature E), and the second in L* ~5.2 (feature F). These local loss processes contributed to the electron flux dropout during the influence of the ICME's magnetosheath, which is attributed to the pitch angle scattering mechanisms by EMIC and chorus waves, respectively, as discussed in Sections 4.2.2 and 4.2.3 (see Aseev et al., 2017; Iles et al., 2006; W. Li & Hudson 2019; Shprits, Horne, et al., 2017). The local flux increase is also observed between L* ~4.8 and ~5.2 (feature D), driven by the chorus waves, as discussed in previous sections. Figure 14b (outbound) presents a local loss between both L* ~4.8 and 5.3 (green curve—from 22:10 UT), named here as feature G which is also observed for $\mu = 2,000$ and 2,500 MeV/G (Figures S7 and S8).

5.3. Event Timeline

The study's main results suggest that the interplanetary coronal mass ejections' structures and their sheath can trigger the drivers to generate the different dynamic mechanisms responsible for the radiation belt population variability. Thereby, we use a timeline in Figure 15 to show each driver able to generate these different dynamic mechanisms responsible by high-energy flux dropout along the time.

ULF wave activities measured on the ground (IMAGE network) are represented for the solid green line. Chorus and EMIC wave activities measured in situ (Van Allen Probe A) are designated by both the blue and red solid lines, respectively. RMP (magnetopause standoff distance) minimum is represented for the solid brown line. The blue, yellow, and light pink boxes represent the flux dropout period after 21:56 UT (L* = 5.2), the flux dropout period after 02:39 UT (L* = 4.6), and the period without flux dropout, respectively. S1 and
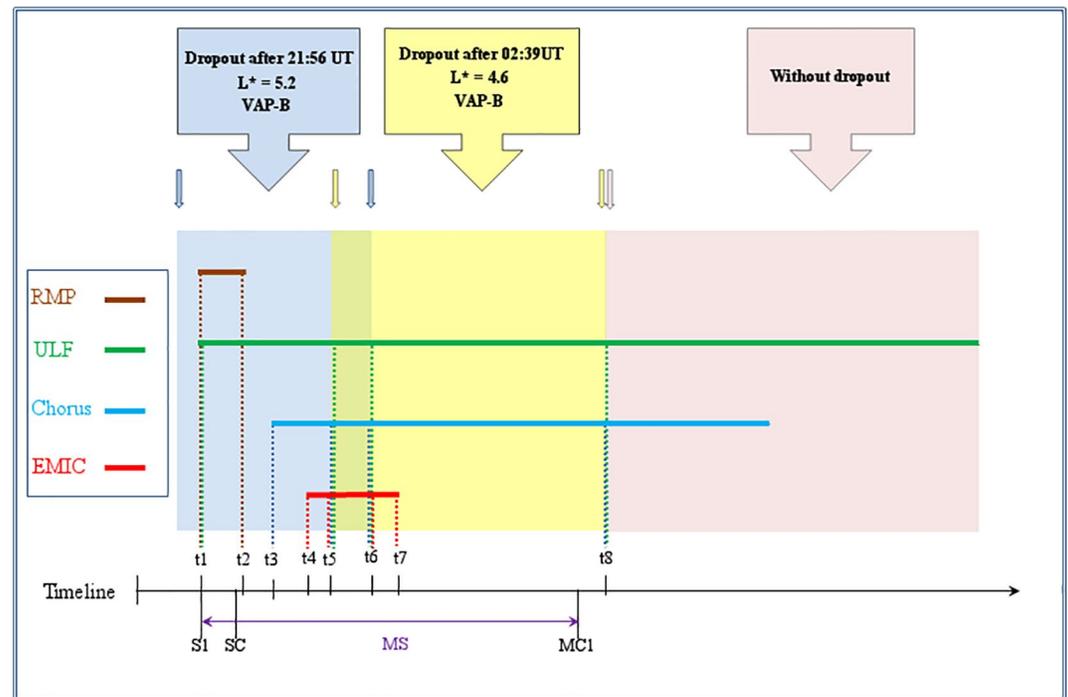
Figure 15. Timeline of the drivers that generate the different dynamic mechanisms responsible by high-energy electron flux dropout observed under the influence of the ICME's sheath region. ULF wave activities measured on the ground (IMAGE network) are represented for the solid green line. Chorus and EMIC wave activities measured in situ (Van Allen Probe A) are designated by both the blue and red solid lines, respectively. RMP (magnetopause standoff distance) minimum is represented for the solid brown line. The blue, yellow, and light pink boxes represent the flux dropout period after 21:56 UT ($L^* = 5.2$), the flux dropout period after 02:39 UT ($L^* = 4.6$), and the period without flux dropout, respectively. S1 and SC indicate the occurrence of the interplanetary shock and the sudden commencement impulse, respectively. MS and MC1 indicate the ICME's magnetosheath, and the boundary of the following interplanetary magnetic cloud, respectively. EMIC, electromagnetic ion cyclotron; ICME, interplanetary counterpart of a solar coronal mass ejection; ULF, ultralow frequency.

SC indicate the occurrence of the interplanetary shock and the sudden commencement impulse, respectively. MS and MC1 indicate the ICME's magnetosheath, and the boundary of the subsequent interplanetary magnetic cloud, respectively.

The high-energy electron flux dropout observed after 21:56 UT (box blue) occurred under the influence of the following dynamic mechanisms:

(1) Magnetopause shadowing due to the magnetopause compression (t1–t2)
(2) Outward radial diffusion driven by ULF waves (t1–t6)
(3) Pitch angle scattering driven by chorus waves (t3–t6), and
(4) Pitch angle scattering driven by EMIC waves (t4–t6)

The high-energy electron flux dropout observed after 02:39 UT (box yellow) occurred under the influence of the following dynamic mechanisms:

(1) Outward radial diffusion driven by ULF waves (t5–t8)
(2) Pitch angle scattering driven by chorus waves (t5–t8), and
(3) Pitch angle scattering driven by EMIC waves (t5–t7)

Although the ULF and chorus waves presented the activities after t8, the wave-particle interaction does not look efficient to cause variability in the outer radiation belt flux (box light pink).

6. Concluding Remarks

Our results, in this study, suggest that the structures of the interplanetary coronal mass ejections can trigger the drivers to generate the different dynamic mechanisms responsible for the radiation belt population variability. We found that the following processes may have contributed to the high-energy electron flux dropout observed during the turbulent ICME's sheath region."

- The interplanetary shock S1 caused a strong compression in the magnetopause, as estimated by the SWMF/BATS-R-US global MHD model and by the empirical Shue et al. (1998) model. Magnetopause stand-off distance reached L = 6, which confirms that the magnetopause shadowing mechanism contributed to this high-energy electron flux dropout in the study
- Observational ground-based data from the IMAGE network confirm strong ULF wave activity during the ICME's sheath region, decreasing significantly in the magnetic cloud region
- The global MHD SWMF/BATS-R-US simulation results suggest that the ULF waves contributed to this high-energy electron flux dropout, once the power of both $B\|$ and $E\varphi$ were considerably strong in the analyzed 1.5 h interval
- The radial diffusion coefficient D_{LL} was calculated through an analytical expression derived by Ozeke et al. (2014), in which the results suggest that the outward radial diffusion mechanism contributed to this high-energy electron flux dropout
- Observational data from Van Allen Probes confirm both EMIC and chorus wave activities during the ICME's sheath region. However, EMIC waves are detected during the period when the Earth's magnetosphere is under the influence of only the ICME's sheath, while the chorus waves are also detected in the subsequent magnetic cloud period
- The minimum resonance energy estimate as 1.2 MeV suggests that the EMIC wave packets detected may resonantly interact with particles ≥1.2 MeV. Consequently, we suggest that the pitch angle scattering mechanism driven by EMIC waves contributed to the high-energy electron flux dropout during this interval
- The cyclotron resonant interaction between particles and chorus waves estimated through the analyses of the chorus subelements (∼01:55:30 UT to 02:00:00 UT on July 20, 2016), has shown that the pitch angle scattering by chorus wave-particle interaction may have contributed to this high-energy electron flux dropout
- The cyclotron resonant interaction between particles and chorus waves estimated analytically under the quasilinear approximation (∼01:55:30 UT to 02:00:00 UT on July 20, 2016), has shown that the wave amplitude leads to significant pitch-angle scattering with the characteristic time scales of about an hour for 1 MeV electrons. The wave obliqueness may have led to scattering time scales of tens of minutes. Thereby, this result confirms the contribution of the pitch angle scattering by chorus waves in this high-energy electron flux dropout
- The PAD shows the high-energy flux dropout in the pitch angles between 50° and 130° in three periods, concomitant to the significant signatures of the ULF waves. Thereby, we conclude that ULF waves' outward radial diffusion is responsible for this shape in PAD
- The PAD also shows the high-energy flux dropout in the pitch angles between 130°–160° and 20°–50°, which are concomitant with chorus and EMIC waves. Thereby, we conclude that the pitch angle scattering driven by the chorus and EMIC waves is responsible for PAD's shape
- The PhSD profiles in the inbound regions considering μ = 1500 MeV/G and K = 0.041 $G^{1/2}$RE confirms that the outward radial diffusion mechanism contributed to the high-energy flux dropout from $L^* = 4$. The PhSD profiles in the outbound regions confirms that the magnetopause shadowing mechanism contributed to the high-energy electron flux dropout from $L^* = 5.3$
- The PhSD profiles in the inbound regions considering μ = 1500 MeV/G and K = 0.128G1/2RE confirm the pitch angle scattering mechanisms by EMIC and chorus waves contributed to the high-energy flux dropout in $L^* \sim 4.8$ and ~ 5.2. The PhSD profiles in the outbound regions for μ = 1500 MeV/G and second K = 0.128G1/2RE confirm a local loss between $L^* \sim 4.8$ and 5.3

Data Availability Statement

All the data used are available at: ECT: https://www.rbsp-ect.lanl.gov/data_pub/, SWS/SEM/HEPD: https://doi.org/10.5281/zenodo.4111070, EMFISIS: https://emfisis.physics.uiowa.edu/Flight/, ACE: http://www.srl.caltech.edu/ACE/ASC/DATA/browse-data/, IMAGE: http://supermag.jhuapl.edu/mag/, WIND: https://cdaweb.gsfc.nasa.gov

References

Agapitov, O., Artemyev, A., Krasnoselskikh, V., Khotyaintsev, Y. V., Mourenas, D., Breuillard, H., et al. (2013). Statistics of whistler mode waves in the outer radiation belt: Cluster STAFF-SA measurements. *Journal of Geophysical Research: Space Physics*, *118*, 3407–3420. https://doi.org/10.1002/jgra.50312

Agapitov, O. V., Artemyev, A. V., Mourenas, D., Mozer, F. S., & Krasnoselskikh, V. (2015). Empirical model of lower band chorus wave distribution in the outer radiation belt. *Journal of Geophysical Research: Space Physics*, *120*(12), JA021829. https://doi.org/10.1002/2015JA021829

Agapitov, O., Krasnoselskikh, V., Khotyaintsev, Y. V., & Rolland, G. (2012). Correction to "A statistical study of the propagation characteristics of whistler waves observed by Cluster". *Geophysical Research Letters*, *39*, L24102. https://doi.org/10.1029/2012GL054320

Agapitov, O., Mourenas, D., Artemyev, A., Hospodarsky, G., & Bonnell, J. W. (2019). Time scales for electron quasi-linear diffusion by lower-band chorus waves: The effects of $\omega pe/\Omega ce$ dependence on geomagnetic activity. *Geophysical Research Letters*, *46*(12), 6178–6187. https://doi.org/10.1029/2019GL083446

Agapitov, O. V., Mourenas, D., Artemyev, A. V., Mozer, F. S., Hospodarsky, G., Bonnell, J., & Krasnoselskikh, V. (2018). Synthetic empirical chorus wave model from combined Van Allen probes and cluster statistics. *Journal of Geophysical Research: Space Physics*, *123*(1), 297–314. https://doi.org/10.1002/2017JA024843

Alves, L. R., Da Silva, L. A., Souza, V. M., Sibeck, D. G., Jauer, P. R., Vieira, L. E. A., et al. (2016). Outer radiation belt dropout dynamics following the arrival of two interplanetary coronal mass ejections. *Geophysical Research Letters*, *43*, 978–987. https://doi.org/10.1002/2015GL067066

Alves, L. R., Souza, V. M., Jauer, P. R., Da Silva, L. A., Medeiros, C., Braga, C. R., et al. (2017). The role of solar wind structures in the generation of ULF waves in the inner magnetosphere. *Solar Physics*, *292*.

Artemyev, A., Agapitov, O., Mourenas, D., Krasnoselskikh, V., Shastun, V., & Mozer, F. (2016). Oblique whistler-mode waves in the earth's inner magnetosphere: energy distribution, origins, and role in radiation belt dynamics. *Space Science Reviews*, *200*(1–4), 261–355. https://doi.org/10.1007/s11214-016-0252-5

Artemyev, A. V., Agapitov, O. V., Mourenas, D., Krasnoselskikh, V., & Zelenyi, L. M. (2013). Storm-induced energization of radiation belt electrons: Effect of wave obliquity. *Geophysical Research Letters*, *40*(16), 4138–4143. https://doi.org/10.1002/grl.50837

Aseev, N. A., Shprits, Y. Y., Drozdov, A. Y., Kellerman, A. C., Usanova, M. E., Wang, D., & &Zhelavskaya, I. S. (2017). Signatures of ultra-relativistic electron loss in the heart of the outer radiation belt measured by Van Allen Probes. *Journal of Geophysical Research: Space Physics*, *122*, 10102–10111. https://doi.org/10.1002/2017JA024485

Baker, D. N., Blake, J. B., Callis, L. B., Cummings, J. R., Hovestadt, D., Kanekal, S., et al. (1994). Relativistic electron acceleration and decay time scales in the inner and outer radiation belts: SAMPEX. *Geophysical Research Letters*, *21*(6), 409–412. https://doi.org/10.1029/93GL03532

Baker, D. N., Hoxie, V. C., Batiste, S., Bolton, M., Li, X., Elkington, S. R., et al. (2013). The relativistic electron-proton telescope (REPT) instrument on board the Radiation Belt Storm Probes (RBSP) spacecraft: Characterization of Earth's Radiation belt high-energy particle populations. *Space Science Reviews*, *179*(1–4), 337–381.

Baker, D. N., Jaynes, A. N., Kanekal, S. G., Foster, J. C., Erickson, P. J., Fennell, J. F., et al. (2016). Highly relativistic radiation belt electron acceleration, transport, and loss: Large solar storm events of March and June 2015. *Journal of Geophysical Research: Space Physics*, *121*(7), 6647–6660. https://doi.org/10.1002/2016JA022502

Baker, D. N., Jaynes, A. N., Li, X., Henderson, M. G., Kanekal, S. G., Reeves, G. D., et al. (2014). Gradual diffusion and punctuated phase space density enhancements of highly relativistic electrons: Van Allen Probes observations. *Geophysical Research Letters*, *41*, 1351–1358. https://doi.org/10.1002/2013GL058942

Baker, D. N., & Kanekal S. G. (2008). Solar cycle changes, geomagnetic variations, and energetic particle properties in the inner magnetosphere, *Journal of Atmospheric and Solar-Terrestrial Physics*, *70*(2–4), 195–206. http://dx.doi.org/10.1016/j.jastp.2007.08.031

Blake, J. B., Carranza, P. A., Claudepierre, S. G., Clemmons, J. H., Crain Jr, W. R., Dotan, Y., et al. (2013). The magnetic electron ion spectrometer (MagEIS) instruments aboard the radiation belt storm probes (RBSP) spacecraft. *Space Science Reviews*, *179*, 383–421. https://doi.org/10.1007/s11214-013-9991-8

Bortnik, J., & Thorne, R. M. (2007). The dual role of ELF/VLF chorus waves in the acceleration and precipitation of radiation belt electrons. *Journal of Atmospheric and Solar-Terrestrial Physics*, *69*, 378–386. https://doi.org/10.1016/j.jastp.2006.05.030

Boyd, A. J., Spence, H. E., Huang, C.-L., Reeves, G. D., Baker, D. N., Turner, D. L., et al. (2016). Statistical properties of the radiation belt seed population. *Journal of Geophysical Research: Space Physics*, *121*, 7636–7646. https://doi.org/10.1002/2016JA022652

Boyd, A. J., Turner, D. L., Reeves, G. D., Spence, H. E., Baker, D. N., & Blake, J. B. (2018). What causes radiation belt enhancements: A survey of the Van Allen probes era. *Geophysical Research Letters*, *45*, 5253–5259. https://doi.org/10.1029/2018GL077699

Brautigam, D. H., Ginet, G. P., Albert, J. M., Wygant, J. R., Rowland, D. E., Ling, A., & Bass, J. (2005). CRRES electric field power spectra and radial diffusion coefficients. *Journal of Geophysical Research*, *110*, A02214. https://doi.org/10.1029/2004JA010612

Burlaga, L. F.; Sittler, E.; Mariani, F. & Schwenn, R. (1981) Magnetic loop behind an interplanetary shock: Voyager, Helios and IMP-8 observations. *Journal of Geophysical Research*, *86*(A8), 6673–6684.

Burton, R. K., & Holzer, R. E. (1974). The origin and propagation of chorus in the outer magnetosphere. *Journal of Geophysical Research*, *79*, 1014–1023.

Cane, H. V., & Richardson, I. G. (2003). Interplanetary coronal mass ejections in the near-Earth solar wind during 1996–2002. *Journal of Geophysical Research*, *108*(A4), 1156. https://doi.org/10.1029/2002JA009817

Claudepierre, S. G., Elkington, S. R., & Wiltberger, M. (2008). Solar wind driving of magnetospheric ULF waves: Pulsations driven by velocity shear at the magnetopause. *Journal of Geophysical Research*, *113*, A05218. https://doi.org/10.1029/2007JA012890

Claudepierre, S. G., Hudson, M. K., Lotko, W., Lyon, J. G., & Denton, R. E. (2010). Solar wind driving of magnetospheric ULF waves: Field line resonances driven by dynamic pressure fluctuations. *Journal of Geophysical Research*, *115*, A11202. https://doi.org/10.1029/2010JA015399

Claudepierre, S. G., Wiltberger, M., Elkington, S. R., Lotko, W., & Hudson, M. K. (2009). Magnetospheric cavity modes driven by solar wind dynamic pressure fluctuations. *Geophysical Research Letters*, *36*, L13101. https://doi.org/10.1029/2009GL039045

Cornwall, J. M. (1965). Cyclotron instabilities and electromagnetic emission in the ultra low frequency and very low frequency ranges. *Journal of Geophysical Research*, *70*(1), 61–69. https://doi.org/10.1029/JZ070i001p00061

Da Silva, L. A., Sibeck, D., Alves, L. R., Souza, V. M., Jauer, P. R., Claudepierre, S. G., et al. (2019). Contribution of ULF wave activity to the global recovery of the outer radiation belt during the passage of a high-speed solar wind stream observed in September 2014. *Journal of Geophysical Research: Space Physics*, *124*, 1660–1678. https://doi.org/10.1029/2018JA026184

De Zeeuw, D. L., Sazykin, S., Wolf, R., Gombosi, T., Ridley, A., & Tóth, G. (2004). Coupling of a global MHD code and an inner magnetosphere model: Initial results. *Journal of Geophysical Research*, *109*, A12219. https://doi.org/10.1029/2003JA010366

Denton, R. E., LaBelle, J., & Zhu, X. (2002). Location of Pc 1–2 waves relative to the magnetopause. *Annales Geophysicae*, *20*, 1763–1767. https://doi.org/10.5194/angeo-20-1763-2002

Elkington, S. R. (2006). A review of ULF interactions with radiation belt electrons. In T. Kazue, P. J. Chi, & R. E. Denton (Eds.), Magnetospheric ULF waves: Synthesis and new directions, geophysical monography series 169 (pp. 177–194). Washington, DC: AGU.

Fei, Y., Chan, A. A., Elkington, S. R., & Wiltberger, M. J. (2006). Radial diffusion and MHD particle simulations of relativistic electron transport by ULF waves in the September 1998 storm. *Journal of Geophysical Research*, *111*, A12209. https://doi.org/10.1029/2005JA011211

Gombosi, T. I., Powell, K. G., De Zeeuw, D. L., Clauer, C. R., Hansen, K. C., Manchester, W. B., et al. (2004). Solution-adaptive magnetohydrodynamics for space plasmas: Sun-to-Earth simulations. *Computing in Science & Engineering*, *6*, 14–35. http://dx.doi.org/10.1109/MCISE.2004.1267603

Gonzalez, W., Joselyn, J., Kamide, Y., Kroehl, H., Rostoker, G., Tsurutani, B., & Vasyliunas, V. (1994). What is a geomagnetic storm? *Journal of Geophysical Research*, *99*(A4), 5771–5792.

Green, J. C., & Kivelson, M. G. (2004). Relativistic electrons in the outer radiation belt: Differentiating between acceleration mechanisms. *Journal of Geophysical Research*, *109*, A03213. https://doi.org/10.1029/2003JA010153

Gurnett, D. A., & O'Brien, B. J. (1964). High-latitude geophysical studies with satellite Injun 3: 5. Very-low-frequency electromagnetic radiation. *Journal of Geophysical Research*, *69*(1), 65–89. https://doi.org/10.1029/JZ069i001p00065

Halford, A. J., Fraser, B. J., & Morley, S. K. (2010). EMIC wave activity during geomagnetic storm and nonstorm periods: CRRES results. *Journal of Geophysical Research*, *115*, A12248. https://doi.org/10.1029/2010JA015716

Halford, A. J., Fraser, B. J., Morley, S. K., Elkington, S. R., & Chan, A. A. (2016). Dependence of EMIC wave parameters during quiet, geomagnetic storm, and geomagnetic storm phase times. *Journal of Geophysical Research: Space Physics*, *121*, 6277–6291. https://doi.org/10.1002/2016JA022694

Hartley, D. P., & Denton, M. H. (2014). Solving the radiation belt riddle. *Astronomy and Geophysics*, *55*(6), 617–620. https://doi.org/10.1093/astrogeo/atu247

Hasegawa, A. (1969). Drift mirror instability in the magnetosphere. *Physics of Fluids*, *12*, 2642.

Helliwell, R. A. (1969). Low-frequency waves in the magnetosphere. *Review of Geophysics*, *71*(1–2), 281–303.

Herrera, D., Maget, V. F., & Sicard-Piet, A. (2016). Characterizing magnetopause shadowing effects in the outer electron radiation belt during geomagnetic storms. *Journal of Geophysical Research: Space Physics*, *121*, 9517–9530. https://doi.org/10.1002/2016JA022825

Horne, R. B. (2002). The contribution of wave-particle interactions to electron loss and acceleration in the Earth's radiation belts during geomagnetic storms. In W. R. Stone (Ed.), *URSI review of radio science 1999-2002* (pp. 801–828). New York, NY: Wiley.

Horne, R. B., Glauert, S. A., & Thorne, R. M. (2003). Resonant diffusion of radiation belt electrons by whistler-mode chorus. *Geophysical Research Letters*, *30*(9), 46-1–46-4. https://doi.org/10.1029/2003GL016963

Horne, R. B., & Thorne, R. M. (1993). On the preferred source location for the convective amplification of ion cyclotron waves. *Journal of Geophysical Research*, *98*, 9233.

Horne, R. B., & Thorne, R. M. (1998). Potential waves for relativistic electron scattering and stochastic acceleration during magnetic storms. *Geophysical Research Letters*, *25*, 3011–3014. https://doi.org/10.1029/98GL01002

Huang, C.-L., Spence, H. E., Hudson, M. K., & Elkington, S. R. (2010). Modeling radiation belt radial diffusion in ULF wave fields: 2. Estimating rates of radial diffusion using combined MHD and particle codes. *Journal of Geophysical Research*, *115*, A06216. https://doi.org/10.1029/2009JA014918

Iles, R. H. A., Meredith, N. P., Fazakerley, A. N., & Horne, R. B. (2006). Phase space density analysis of the outer radiationbelt energetic electron dynamics. *Journal of Geophysical Research*, *111*, A03204. https://doi.org/10.1029/2005JA011206

Jauer, P. R., Wang, C., Souza, V. M., Alves, M. V., Alves, L. R., Pádua, M. B., et al. (2019). A global magnetohydrodynamic simulation study of ultra-low-frequency wave activity in the inner magnetosphere: Corotating interaction region + Alfvénic fluctuations. *The Astrophysical Journal*, *886*(16), 59. https://doi.org/10.3847/1538-4357/ab4db5

Jordanova, V. K., Welling, D. T., Zaharia, S. G., Chen, L., & Thorne, R. M. (2012). Modeling ring current ion and electron dynamics and plasma instabilities during a high-speed driven storm. *Journal of Geophysical Research*, *117*, A00L08. https://doi.org/10.1029/2011JA017433

Kalliokoski, M. M. H., Kilpua, E. K. J., Osmane, A., Turner, D. L., Allison, N. J., Turc, L., et al. (2020). Outer radiation belt and inner magnetospheric response to sheath regions of coronal mass ejections: A statistical analysis. *Annales Geophysicae*, *38*, 683–701. https://doi.org/10.5194/angeo-38-683-2020

Kamiya, K., Seki, K., Saito, S., Amano, T., & Miyoshi, Y. (2018). Formation of butterfly pitch angle distributions of relativistic electrons in the outer radiation belt with a monochromatic Pc5 wave. *Journal of Geophysical Research: Space Physics*, *123*, 4679–4691. https://doi.org/10.1002/2017JA024764

Kang, S.-B., Fok, M.-C., Glocer, A., Min, K.-W., Choi, C.-R., Choi, E., & Hwang, J. (2016). Simulation of a rapid dropout event for highly relativistic electrons with the RBE model. *Journal of Geophysical Research: Space Physics*, *121*, 4092–4102. https://doi.org/10.1002/2015JA021966

Kasahara, S., Miyoshi, Y., Yokota, S., Mitani, T., Kasahara, Y., Matsuda, S., et al. (2018). Shinohara. Pulsating aurora from electron scattering by chorus waves. *Nature*, *554*, 337–340. https://doi.org/10.1038/nature25505

Kennel, C. F., & Petschek, H. E. (1966). Limit on stably trapped particle fluxes. *Journal of Geophysical Research*, *71*, 1–28. https://doi.org/10.1029/JZ071i001p00001

Kilpua, E. K. J., Isavnin, A., Vourlidas, A., Koskinen, H. E. J., & Rodriguez, L. (2013). On the relationship between interplanetary coronal mass ejections and magnetic clouds. *Annales Geophysicae*, *31*, 1251–1265. https://doi.org/10.5194/angeo-31-1251-2013

Kilpua, E., Koskinen, H. E. J., & Pulkkinen, T. I. (2017). Coronal mass ejections and their sheath regions in interplanetary space. *Living Reviews in Solar Physics*, *14*, 5. https://doi.org/10.1007/s41116-017-0009-6

Kim, K. C., Lee, D. Y., Kim, H. J., Lyons, L. R., Lee, E. S., Öztürk, M. K., & Choi, C. R. (2008). Numerical calculations of relativistic electron drift loss effect. *Journal of Geophysical Research*, *113*(A9), A09212. https://doi.org/10.1029/2007JA013011

Kivelson, M. G., & Southwood, D. J. (1985). Charged particle behavior in low-frequency geomagnetic pulsations 4. Compressional waves. *Journal of Geophysical Research*, *90*, (A2), 1486–1498. https://doi.org/10.1029/JA090iA02p01486

Kletzing, C. A., Kurth, W. S., Acuna, M., MacDowall, R. J., Torbert, R. B., Averkamp, T., et al. (2013). The electric and magnetic field instrument suite and integrated science (EMFISIS) on RBSP. *Space Science Reviews*, *179*(1–4), 127–181. https://doi.org/10.1007/s11214-013-9993-6

Komar, C. M., Glocer, A., Hartinger, M. D., Murphy, K. R., Fok, M.-C. H., & Kang, S.-B. (2017). Electron drift resonance in the MHD-coupled comprehensive inner magnetosphere-ionosphere model. *Journal of Geophysical Research: Space Physics*, *122*(12), 12006–12018. https://doi.org/10.1002/2017JA024163

Kress, B. T., Hudson, M. K., Looper, M. D., Albert, J., Lyon, J. G., & Goodrich, C. C. (2007). Global MHD test particle simulations of >10 MeV radiation belt electrons during storm sudden commencement. *Journal of Geophysical Research*, *112*, A09215. https://doi.org/10.1029/2006JA012218

Lakhina, G. S., Tsurutani, B. T., Verkhoglyadova, O. P., & Pickett, J. S. (2010). Pitch angle transport of electrons due to cyclotron interactions with the coherent chorus subelements. *Journal of Geophysical Research*, *115*, A00F15. https://doi.org/10.1029/2009JA014885

Lauben, D. S., Inan, U. S., Bell, T. F., & Gurnett, D. A. (2002). Source characteristics of ELF/VLF chorus. *Journal of Geophysical Research*, *107*(A12), 1429. https://doi.org/10.1029/2000JA003019

LeDocq, M. J., Gurnett, D. A., & Hospodarsky, G. B. (1998). Chorus source locations from VLF Poynting flux measurements with the POLAR spacecraft. *Geophysical Research Letters*, *25*, 4063–4066.

Li, X., Baker, D. N., Temerin, M., Cayton, T. E., Reeves, E. G. D., Christensen, R. A., et al. (1997). Multisatellite observations of the outer zone electron variation during the November 3–4, 1993, magnetic storm. *Journal of Geophysical Research*, *102*, 14123–14140. https://doi.org/10.1029/97JA01101

Li, W., & Hudson, M. K. (2019). Earth's Van Allen radiation belts: From discovery to the Van Allen Probes era. *Journal of Geophysical Research: Space Physics*, *124*(11), 8319–8351. https://doi.org/10.1029/2018JA025940

Li, W., Mourenas, D., Artemyev, A. V., Agapitov, O. V., Bortnik, J., Albert, J. M., et al. (2014). Evidence of stronger pitch angle scattering loss caused by oblique whistler-mode waves as compared with quasi-parallel waves. *Geophysical Research Letters*, *41*(17), GL061260. https://doi.org/10.1002/2014GL061260

Mann, I. R., Wright, A. N., Mills, K. J., & Nakariakov, V. M. (1999). Excitation of magnetospheric waveguide modes by magnetosheath flows. *Journal of Geophysical Research*, *104*(A1), 333–353.

Mauk, B. H., Fox, N. J., Kanekal, S. G., Kessel, R. L., Sibeck, D. G., & Ukhorskiy, A. (2012). Science objectives and rationale for the radiation belt storm probes mission. *Space Science Reviews*, *179*, 3–27. https://doi.org/10.1007/s11214-012-9908-y

McCollough, J. P., Elkington, S. R., Usanova, M. E., Mann, I. R., Baker, D. N., & Kale, Z. C. (2010). Physical mechanisms of compressional EMIC wave growth. *Journal of Geophysical Research*, *115*, A10214. https://doi.org/10.1029/2010JA015393

Medeiros, C., Souza, V. M., Vieira, L. E. A., Sibeck, D. G., Halford, A. J., Kang, S.-B., et al. (2019). On the contribution of EMIC waves to the reconfiguration of the relativistic electron butterfly pitch angle distribution shape on 2014 September 12—A case study. *The Astrophysical Journal*, *872*(17), 36.

Meredith, N. P., Horne, R. B., & Anderson, R. R. (2001), Substorm dependence of chorus amplitudes: Implications for the acceleration of electrons to relativistic energies, *Journal of Geophysical Research*, *106*(A7), 13165–13178. https://doi.org/10.1029/2000JA900156

Meredith, N. P., Horne, R. B., Kersten, T., Fraser, B. J., & Grew, R. S. (2014). Global morphology and spectral properties of EMIC waves derived from CRRES observations. *Journal of Geophysical Research: Space Physics*, *119*, 5328–5342. https://doi.org/10.1002/2014JA020064

Morley, S. K., Friedel, R. H. W., Spanswick, E. L., Reeves, G. D., Steinberg, J. T., Koller, J., et al. (2010). Dropouts of the outer electron radiation belt in response to solar wind stream interfaces: Global positioning system observations. *Proceedings of the Royal Society A*, *466*, 3329–3350. https://doi.org/10.1098/rspa.2010.0078

Mourenas, D., Artemyev, A. V., Agapitov, O. V., & Krasnoselskikh, V. (2014). Consequences of geomagnetic activity on energization and loss of radiation belt electrons by oblique chorus waves. *Journal of Geophysical Research: Space Physics*, *119*, 2775–2796. https://doi.org/10.1002/2013JA019674

Murphy, K. R., Watt, C. E. J., Mann, I. R., Jonathan Rae, I., Sibeck, D. G., Boyd, A. J., et al. (2018). The global statistical response of the outer radiation belt during geomagnetic storms. *Geophysical Research Letters*, *45*, 3783–3792. https://doi.org/10.1002/2017GL076674

Nagai, T. (1988). "Space weather forecast": Prediction of relativistic electron intensity at synchronous orbit. *Geophysical Research Letters*, *15*(5), 425–428. https://doi.org/10.1029/GL015i005p00425

Ni, B., Bortnik, J., Thorne, R. M., Ma, Q., & Chen, L. (2013). Resonant scattering and resultant pitch angle evolution of relativistic electrons by plasmaspheric hiss. *Journal of Geophysical Research: Space Physics*, *118*, 7740–7751. https://doi.org/10.1002/2013JA019260

Ni, B., Cao, X., Zou, Z., Zhou, C., Gu, X., Bortnik, J., et al. (2015). Resonant scattering of outer zone relativistic electrons by multiband EMIC waves and resultant electron loss time scales. *Journal of Geophysical Research: Space Physics*, *120*, 7357–7373. https://doi.org/10.1002/2015JA021466

Ni, B., Hua, M., Zhou, R., Yi, J., & Fu, S. (2017). Competition between outer zone electron scattering by plasmaspheric hiss and magnetosonic waves. *Geophysical Research Letters*, *44*, 3465–3474. https://doi.org/10.1002/2017GL072989

Nishimura, Y., Bortnik, J., Li, W., Thorne, R. M., Chen, L., Lyons, L. R., et al. (2011). Multievent study of the correlation between pulsating aurora and whistler mode chorus emissions. *Journal of Geophysical Research*, *116*, A11221.

Nishimura, Y., Bortnik, J., Li, W., Thorne, R. M., Lyons, L. R., Angelopoulos, V., et al. (2010). Identifying the driver of pulsating aurora. *Science*, *330*(6000), 81–84.

Ni, B., Thorne, R. M., Shprits, Y. Y., & Bortnik, J. (2008). Resonant scattering of plasma sheet electrons by whistler-mode chorus: Contribution to diffuse auroral precipitation. *Geophysical Research Letters*, *35*, L11106. https://doi.org/10.1029/2008GL034032

Northrop, T. G., & Teller, E. (1960). Stability of the adiabatic motion of charged particles in the Earth's field. *Physical Review*, *117*(1), 215–225. https://doi.org/10.1103/PhysRev.117.215

Ogilvie, K. W., Chornay, D. J., Fritzenreiter, R. J., Hunsaker, F., Keller, J., Lobell, J., et al. (1995). SWE, a comprehensive plasma instrument for the WIND spacecraft. *Space Science Reviews*, *71*, 55–77. https://doi.org/10.1007/BF00751326

Ozeke, L. G., Mann, I. R., Murphy, K. R., Jonathan Rae, I., & Milling, D. K. (2014). Analytic expressions for ULF wave radiation belt radial diffusion coefficients. *Journal of Geophysical Research: Space Physics*, *119*, 1587–1605. https://doi.org/10.1002/2013JA019204

Paulikas, G. A., & Blake, J. B. (1979). Effects of the solar wind on magnetospheric dynamics: Energetic electrons at the synchronous orbit. In *Quantitative modeling of magnetospheric processes, geophysical monography series 21* (180–202). Washington, DC: AGU.

Perry, K. L., Hudson, M. K., & Elkington, S. R. (2005). Incorporating spectral characteristics of Pc5 waves into three-dimensional radiation belt modeling and the diffusion of relativistic electrons. *Journal of Geophysical Research*, *110*, A03215. https://doi.org/10.1029/2004JA010760

Ponomarev, E. A., Sedykh, P. A., & Urbanovich, V. D. (2006). Bow shock as a power source for magnetospheric processes. *Journal of Atmospheric and Solar-Terrestrial Physics*, *68*, 685–690.

Powell, K. G., Roe, P. L. T. J., Linde, T. I., Gombosi, & De Zeeuw, D. L. (1999). A solution-adaptive upwind scheme for ideal magnetohydrodynamics. *Journal of Computational Physics*, *154*, 284–309. https://doi.org/10.1006/jcph.1999.6299

Reeves, G. D., Spence, H. E., Henderson, M. G., Morley, S. K., Friedel, R. H. W., Funsten, H. O., et al. (2013). Electron acceleration in the heart of the Van Allen radiation belts. *Science*, *341*, 991–994. https://doi.org/10.1126/science.1237743

Ridley, A. J., & Liemohn, M. W. (2002). A model-derived stormtime asymmetric ring current driven electric field description. *Journal of Geophysical Research*, *107*(A8), SMP 2-1–SMP 2-12. https://doi.org/10.1029/2001JA000051

Roederer, J. G. (1968). Experimental evidence on radial diffusion of geomagnetically trapped particles. In B. M. McCormac (Ed.), *Earth's particles and fields* (p. 143–155). New York, NY: Reinhold Book Corp.

Roederer, J. G. (1970). Dynamics of geomagnetically trapped radiation. In J. G. Roederer & J. Zahringer (Eds.), *Physics and chemistry in space* (Vol. 2, pp. 166). Berlin: Springer.

Sandanger, M., Søraas, F., Aarsnes, K., Oksavik, K., & Evans, D. S. (2007). Loss of relativistic electrons: Evidence for pitch angle scattering by electromagnetic ion cyclotron waves excited by unstable ring current protons. *Journal of Geophysical Research*, *112*, A12213. https://doi.org/10.1029/2006JA012138

Schulz, M., & Lanzerotti, L. J. (1974). *Particle diffusion in the radiation belts*. New York, NY: Springer-Verlag.

Shabansky, V. P. (1971). Some processes in the magnetosphere. *Space Science Reviews*, *12*, 299–418. https://doi.org/10.1007/BF00165511

Shprits, Y. Y. (2009). Potential waves for pitch-angle scattering of near equatorially mirroring electrons due to violation of the second adiabatic invariant. *Geophysical Research Letters*, *36*, L12106. https://doi.org/10.1029/2009GL038322

Shprits, Y. Y., Horne, R. B., Kellerman, A. C., & Drozdov, A. Y. (2017). Correspondence: The dynamics of Van Allen belts revisited. *Nature Physics*, *14*, 102–103.

Shprits, Y. Y., Kellerman, A., Aseev, N., Drozdov, A. Y., & Michaelis, I. (2017). Multi-MeV electron loss in the heart of the radiation belts. *Geophysical Research Letters*, *44*, 1204–1209. https://doi.org/10.1002/2016GL072258

Shprits, Y. Y., & Ni, B. (2009). Dependence of the quasi-linear scattering rates on the wave normal distribution of chorus waves. *Journal of Geophysical Research*, *114*, A11205. https://doi.org/10.1029/2009JA014223

Shue, J.-H., Song, P., Russell, C. T., Steinberg, J. T., Chao, J. K., Zastenker, G., et al. (1998). Magnetopause location under extremes solar wind conditions. *Journal of Geophysical Research*, *103*(17), 691.

Sibeck, D. G., McEntire, R. W., Lui, A. T. Y., Lopez, R. E., & Krimigis, S. M. (1987). Magnetic field drift shell splitting: Cause of unusual dayside particle pitch angle distributions during storms and substorms. *Journal of Geophysical Research*, *92*, 13485.

Southwood, D. J., Dungey, J. W., & Etherington, R. J. (1969). Bounce resonant interaction between pulsations and trapped particles. *Planetary and Space Science*, *17*, 349.

Souza, V. M., Lopez, R. E., Jauer, P. R., Sibeck, D. G., Pham, K., Da Silva, L. A., et al. (2017). Acceleration of radiation belt electrons and the role of the average interplanetary magnetic field B_z component in high speed streams. *Journal of Geophysical Research: Space Physics*, *122*, 10084–10101.

Souza, V. M., Medeiros, C., Koga, D., Alves, L. R., Vieira, L. E. A., Dal Lago, A., et al. (2018). Classification of magnetospheric particle distributions via neural networks. In E. Camporeale, S. Wing, & J. Johnson (Eds.), *Machine learning techniques for space weather* (1 ed, Vol. 1, pp. 1–10). Elsevier.

Stone, E. C., Frandsen, A. M., Mewaldt, R. A., Christian, E. R., Margolies, D., Ormes, J. F., & Snow, F. (1998). The advanced composition explorer. *Space Science Reviews*, *86*(1/4), 1–22. https://doi.org/10.1023/A:1005082526237

Storey, L. R. O. (1953). An investigation of whistling atmospherics. *Philosophical Transactions of the Royal Society of London*, *A246*, 113–141.

Summers, D., Ni, B., & Meredith, N. P. (2007). Timescales for radiation belt electron acceleration and loss due to resonant wave-particle interactions: 1. Theory. *Journal of Geophysical Research*, *112*, A04206. https://doi.org/10.1029/2006JA011801

Summers, D., & Thorne, R. (2003). Relativistic electron pitch-angle scattering by electromagnetic ion cyclotron waves during geomagnetic storms. *Journal of Geophysical Research*, *108*(A4), 1143. https://doi.org/10.1029/2002JA009489

Takahashi, K., Russell, C. T., & Anderson, R. R. (1985). ISEE 1 and 2 observations of the spatial structure of a compressional Pc 5 wave. *Geophysical Research Letters*, *12*, 613.

Thorne, R. M. (2010). Radiation belt dynamics: The importance of wave-particle interactions. *Geophysical Research Letters*, *37*, L22107. https://doi.org/10.1029/2010GL044990

Thorne, R. M., & Kennel, C. F. (1971). Relativistic electron precipitation during magnetic storm main phase. *Journal of Geophysical Research*, *76*, 4446–4453. https://doi.org/10.1029/JA076i019p04446

Thorne, R. M., Ni, B., Tao, X., Horne, R. B., & Meredith, N. P. (2010). Scattering by chorus waves as the dominant cause of diffuse auroral precipitation. *Nature*, *467*, 943–946. https://doi.org/10.1038/nature09467

Toffoletto, F. R., Sazykin, S., Spiro, R. W., & Wolf, R. A. (2003). Modeling the inner magnetosphere using the rice convection model (review). *Space Science Reviews*, *108*, 175–196.

Tóth, G., Sokolov, I. V., Gombosi, T. I., Chesney, D. R., Clauer, C. R., De Zeeuw, D. L., et al. (2005). Space weather modeling framework: A new tool for the space science community. *Journal of Geophysical Research*, *110*, A12226. https://doi.org/10.1029/2005JA011126

Tóth, G., van der Holst, B., Sokolov, I. V., Zeeuw, D. L. D., Gombosi, T. I., Fang, F., et al. (2012). Adaptive numerical algorithms in space weather modeling. *Journal of Computational Physics*, *231*(3), 870.

Tsurutani, B. T., & Lakhina, G. S. (2014). An extreme coronal mass ejection and consequences for the magnetosphere and Earth. *Geophysical Research Letters*, *41*, 287–292. https://doi.org/10.1002/2013GL058825

Tsurutani, B. T., & Smith, E. J. (1974). Postmidnight chorus: A substorm phenomenon. *Journal of Geophysical Research*, *79*, 118–127. https://doi.org/10.1029/JA079i001p00118

Tsyganenko, N. A., & Sitnov, M. I. (2005). Modeling the dynamics of the inner magnetosphere during strong geomagnetic storms. *Journal of Geophysical Research*, *110*(A3), A03208. https://doi.org/10.1029/2004JA010798

Turner, D. L., Angelopoulos, V., Li, W., Bortnik, J., Ni, B., Ma, Q., et al. (2014). Competing source and loss mechanisms due to wave-particle interactions in Earth's outer radiation belt during the 30 September to 3 October 2012 geomagnetic storm. *Journal of Geophysical Research: Space Physics*, *119*, 1960–1979. https://doi.org/10.1002/2014JA019770

Turner, D. L., Angelopoulos, V., Li, W., Hartinger, M. D., Usanova, M., Mann, I. R., et al. (2013). On the storm-time evolution of relativistic electron phase spacedensity in Earth's outer radiation belt. *Journal of Geophysical Research: Space Physics*, *118*, 2196–2212. https://doi.org/10.1002/jgra.50151

Turner, D. L., Morley, S. K., Miyoshi, Y., Ni, B., & Huang, C.-L. (2012). Outer radiation belt flux dropouts: Current understanding and unresolved questions in: Dynamics of the Earth's radiation belts and inner magnetosphere. *Geophysical Monograph Series*, *199*. https://doi.org/10.1029/2012GM001310

Turner, D. L., & Ukhorskiy, A. Y. (2019). Outer radiation belt losses by magnetopause incursions and outward radial transport: New insight and outstanding questions from the Van Allen Probes era. *The dynamic loss of Earth's radiation belts from loss in the magnetosphere to particle precipitation in the atmosphere* (Chapter 1, pp. 1–28). Elsevier Inc. https://doi.org/10.1016/b978-0-12-813371-2.00001-9

Tu, W., Selesnick, R., Li, X., & Looper, M. (2010). Quantification of the precipitation loss of radiation belt electrons observed by SAMPEX. *Journal of Geophysical Research*, *115*, A07210. https://doi.org/10.1029/2009JA014949

Ukhorskiy, A. Y., Anderson, B. J., Takahashi, K., & Tsyganenko, N. A. (2006). Impact of ULF oscillations in solar wind dynamic pressure on the outer radiation belt electrons. *Geophysical Research Letters*, *33*, L06111. https://doi.org/10.1029/2005GL024380

Ukhorskiy, A. Y., Sitnov, M. I., Millan, R. M., & Kress, B. T. (2011). The role of drift orbit bifurcations in energization and loss of electrons in the outer radiation belt. *Journal of Geophysical Research*, *116*, A09208. https://doi.org/10.1029/2011JA016623

Ukhorskiy, A. Y., Sitnov, M. I., Millan, R. M., Kress, B. T., & Smith, D. C. (2014). Enhanced radial transport and energization of radiation belt electrons due to drift orbit bifurcations. *Journal of Geophysical Research: Space Physics*, *119*, 163–170. https://doi.org/10.1002/2013JA019315

Ukhorskiy, A. Y., Takahashi, K., Anderson, B. J., & Korth, H. (2005). Impact of toroidal ULF waves on the outer radiation belt electrons. *Journal of Geophysical Research*, *110*, A10202. https://doi.org/10.1029/2005JA011017

Usanova, M. E., Drozdov, A., Orlova, K., Mann, I. R., Shprits, Y., Robertson, M. T., et al. (2014). Effect of EMIC waves on relativistic and ultrarelativistic electron populations: Groundbased and Van Allen Probes observations. *Geophysical Research Letters*, *41*, 1375–1381. https://doi.org/10.1002/2013GL059024

Usanova, M. E., Mann, I. R., Bortnik, J., Shao, L., & Angelopoulos, V. (2012). THEMIS observations of electromagnetic ion cyclotron wave occurrence: Dependence on AE, SYMH, and solar wind dynamic pressure. *Journal of Geophysical Research*, *117*, A10218. https://doi.org/10.1029/2012JA018049

Viljanen, A., & Hakkinen, L. (1997). Image magnetometer network. In M. Lockwood, M. N. Wild, & H. J. Opgenoorth (Eds.), *Satellite-ground based coordination sourcebook, ESA publications* (p. 111).

Walt, M., Dessler, A. J., Houghton, J. T., & Rycroft, M. J. (1994). *Introduction to geomagnetically trapped radiation*. Cambridge, UK: Cambridge University Press.

Wilken, B., Goertz, C. K., Baker, D. N., Higbie, P. R., & Fritz, T. A. (1982). The SSC on July 29, 1977 and its propagation within the magnetosphere. *Journal of Geophysical Research*, *87*(A8), 5901–5910. https://doi.org/10.1029/JA087iA08p05901

Wolf, R. A., Harel, M., Spiro, R. W., Voigt, G.-H., Reiff, P. H., & Chen, C. K. (1977). Computer simulation of inner magnetospheric dynamics for the magnetic storm of July 29, 1977. *Journal of Geophysical Research*, *87*, 5949–5962. https://doi.org/10.1029/JA087iA08p05949

Xiang, Z., Tu, W., Li, X., Ni, B., Morley, S. K., & Baker, D. N. (2017). Understanding the mechanisms of radiation belt dropouts observed by Van Allen Probes. *Journal of Geophysical Research: Space Physics*, *122*(10), 9858–9879. https://doi.org/10.1002/2017JA024487

Zhang, X.-J., Li, W., Ma, Q., Thorne, R. M., Angelopoulos, V., Bortnik, J., et al. (2016). Direct evidence for EMIC wave scattering of relativistic electrons in space. *Journal of Geophysical Research: Space Physics*, *121*, 6620–6631. https://doi.org/10.1002/2016JA022521

Zhang, D., Liu, W., Li, X., Sarris, T., Xiao, C., & Wygant, J. R. (2018). Observations of impulsive electric fields induced by interplanetary shock. *Geophysical Research Letters*, *45*, 7287–7296. https://doi.org/10.1029/2018GL078809

Zhang, S. Y., Zhang, X. G., Wang, C. Q., Shen, G. H., Jin, T., Zhang, B. Q., et al. (2014). The geometric factor of high energy protons detector on FY-3 satellite. *Science China Earth Sciences*, *57*(10), 2558–2566.

Zheng, L., Chan, A. A., O'Brien, T. P., Tu, W., Cunningham, G. S., Albert, J. M., & Elkington, S. R. (2016). Effects of magnetic drift shell splitting on electron diffusion in the radiation belts. *Journal of Geophysical Research: Space Physics*, *121*(12), 11,985–12,000. https://doi.org/10.1002/2016JA023438

Zurbuchen, T. H., & Richardson, I. G. (2006). In-situ solar wind and magnetic field signatures of interplanetary coronal mass ejections. *Space Science Reviews*, *123*, 31–43. https://doi.org/10.1007/s11214-006-9010-4